JGR Solid Earth

RESEARCH ARTICLE
10.1029/2025JB032348

Magnetic Mineral Assemblages of Diagenetically Reduced Sediments and Their Contributions to Paleomagnetic Signals

Jiaxi Li[1,2], Toshitsugu Yamazaki[1,3], Masahiko Sato[4], and Junichiro Kuroda[1]

[1]Atmosphere and Ocean Research Institute, The University of Tokyo, Kashiwa, Japan, [2]Technology and Engineering Center for Space Utilization, Chinese Academy of Sciences, Beijing, China, [3]Marine Core Research Institute, Kochi University, Nankoku, Japan, [4]Tokyo University of Science, Tokyo, Japan

Abstract During early diagenesis of marine sediments, iron-bearing minerals undergo a series of redox reactions until they reach equilibrium with reactive chemical components. Paleomagnetic records in the sediments subjected to severe diagenesis can be distorted or lost due to iron mineral dissolution, and hence these sediments were often excluded from paleomagnetic studies without detailed examination. Silicate-hosted magnetic inclusions and hematite are likely more resistive to reductive diagenesis compared with unprotected magnetite. Thus, these minerals have potential for preserving paleomagnetic records in reduced sediments. To better understand this issue, we conducted a paleo- and rock magnetic study of a sediment core taken from the Ontong Java Plateau in the western equatorial Pacific Ocean using various techniques including isothermal remanent magnetization (IRM) component analyses, first-order reversal curve diagrams, low-temperature magnetic measurements, thermal demagnetization of three-component IRM, chemical separation, and electron microscopy. The magnetite dissolution front occurs at 5.7 m in depth in the studied core. Below this horizon, silicate-hosted magnetic inclusions and hematite carry 46%–63% and 21%–34% of saturation IRM, respectively. Depositional remanent magnetization acquisition efficiency of silicate-hosted magnetic inclusions is estimated to be relatively low in the studied core based on the grain sizes of silicate hosts and concentration of magnetic inclusions. It was revealed that magnetostratigraphy and relative paleointensity correlative to the global stacks could still be recovered from the sediments below the dissolution front. Relict hematite may be an important carrier of the paleomagnetic records.

Plain Language Summary Marine sediments potentially preserve continuous records of past geomagnetic field variations, but these precious records can be lost during reductive diagenesis ubiquitous in sediments, because magnetic minerals carrying the records dissolve below a certain depth within sediments. Our study using a sediment core taken from the western equatorial Pacific Ocean revealed that even in sediments suffered from severe reductive diagenesis, hematites as well as magnetites embedded in silicate minerals, which protect the inclusions from dissolution, survive, whereas unprotected magnetite is lost, and that these relict magnetic minerals can preserve past geomagnetic records including variations of the strength of the geomagnetic field. Our study implies that large numbers of legacy sediment cores that were excluded from geomagnetic studies by reason of reductive diagenesis may be useful for future research.

Key Points:

- In sediments suffered from reductive dissolution of magnetite, silicate-hosted magnetic inclusions and hematite survive
- In the studied sediments, DRM acquisition efficiency of magnetic inclusions is relatively low, and hematite is an important carrier of DRM
- Relative paleointensity could be recovered with ARM normalization even from sediments suffered from magnetite dissolution

Supporting Information:

Supporting Information may be found in the online version of this article.

Correspondence to:

T. Yamazaki,
yamazaki@aori.u-tokyo.ac.jp

Citation:

Li, J., Yamazaki, T., Sato, M., & Kuroda, J. (2025). Magnetic mineral assemblages of diagenetically reduced sediments and their contributions to paleomagnetic signals. *Journal of Geophysical Research: Solid Earth*, *130*, e2025JB032348. https://doi.org/10.1029/2025JB032348

Received 30 JUN 2025
Accepted 23 SEP 2025
Corrected 9 OCT 2025

This article was corrected on 9 OCT 2025. See the end of the full text for details.

Author Contributions:

Conceptualization: Toshitsugu Yamazaki
Data curation: Toshitsugu Yamazaki
Formal analysis: Jiaxi Li, Junichiro Kuroda
Funding acquisition: Toshitsugu Yamazaki, Junichiro Kuroda
Investigation: Jiaxi Li, Toshitsugu Yamazaki, Masahiko Sato
Methodology: Jiaxi Li, Masahiko Sato
Project administration: Toshitsugu Yamazaki
Supervision: Toshitsugu Yamazaki

1. Introduction

Marine and lacustrine sediments have potential to preserve continuous records of geomagnetic field variations in the past including relative paleointensity (RPI). Sediments ubiquitously suffer early diagenesis, and at a certain depth in a sedimentary column, reductive dissolution of magnetic minerals starts, as introduced below. This process compromises the preservation of paleomagnetic records (Bloemendal et al., 1992; Karlin & Levi, 1983; Roberts, 2015; Rowan et al., 2009; Yamazaki et al., 2003).

In early diagenesis, sediments undergo a series of chemical changes associated with oxidative degradation of organic matter. Oxidants in sediments are utilized for the oxidation of organic matter according to the decreasing order of free energy yielded by each reaction: oxygen, nitrate, manganese oxides, iron (oxyhydr-)oxides, sulfate, and methane. These oxidants are depleted sequentially until the diagenetic system reaches an equilibrium where either all oxidants or all reactive organic matter are consumed (Berner, 1980, 1981; Froelich et al., 1979; Karlin & Levi, 1983; Roberts, 2015; Rowan et al., 2009). When more energy-producing oxides are depleted, organic matter degradation proceeds with the reduction of Fe^{3+}-bearing minerals to dissolved Fe^{2+} (ferruginous diagenesis),

Validation: Toshitsugu Yamazaki, Masahiko Sato
Visualization: Jiaxi Li
Writing – original draft: Jiaxi Li
Writing – review & editing: Toshitsugu Yamazaki, Masahiko Sato, Junichiro Kuroda

causing dissolution of readily reactive iron minerals such as hydrous ferric oxide, ferrihydrite, and lepidocrocite at the depth known as the iron-redox boundary (Lyle, 1983; Poulton et al., 2004). The loss of these weakly magnetic minerals has little effect on remanent magnetization. Below the ferruginous zone, organic matter degradation proceeds with the reduction of sulfate, releasing dissolved sulfide (H_2S) as a by-product into sedimentary pore water. Sulfate reduction causes dissolution of well-crystallized iron-bearing minerals like magnetite and precipitation of iron sulfides (e.g., pyrite and greigite) (Berner, 1984; Canfield & Berner, 1987). The onset of the pervasive dissolution of magnetite and replacement by paramagnetic pyrite in the sulfate reduction cause a sudden drop in magnetic concentration and remanent magnetization intensity, which define the magnetite dissolution front (Roberts, 2015; Rowan et al., 2009). The reductive dissolution of iron-bearing minerals also leads an increase in their average grain size because finer grains are expected to be dissolved earlier than coarser grains due to their higher surface-to-volume ratio.

Recently, potential of silicate-hosted magnetic inclusions of detrital origin has become recognized as a carrier of the remanent magnetization of the sediments suffered from reductive dissolution of magnetic minerals (Chang, Roberts et al., 2016; Chen et al., 2017; Hong et al., 2019). In such sediments, host silicates protect magnetic inclusions from reductive dissolution, whereas unprotected detrital magnetite and magnetofossil, which are the major carriers of remanent magnetization of marine sediments (e.g., Roberts et al., 2011, 2012; Yamazaki & Ikehara, 2012), are susceptible to dissolution.

The reductive dissolution of magnetic minerals destroys paleomagnetic records at least partly. Sediments with large variations in magnetic mineralogy, concentration, and grain size associated with reductive diagenesis were considered to be unsuitable for relative paleointensity (RPI) estimations in general (King et al., 1983; Tauxe, 1993). On the other hand, rock-magnetic records of diagenetically reduced sediments can help us better understand a sedimentary diagenetic history and underlying information related to paleoceanographic conditions including paleoproductivity (Bouilloux et al., 2013; Chang, Bolton et al., 2016; Larrasoaña et al., 2006; Tarduno & Wilkison, 1996). The extent to which diagenetic reaction proceeds and the corresponding depth at which it occurs are influenced by sedimentation rates and organic matter input, which may be controlled by factors such as orbitally controlled productivity cycles and glacial-interglacial changes. These factors can lead to a cycling of sedimentary environments between oxic and anoxic conditions, resulting in non-steady state diagenesis (Roberts, 2015; Thomson et al., 1984).

Previously, sediment cores suffered from reductive dissolution of magnetic minerals were often excluded from paleomagnetic studies from a preconception that paleomagnetic records would have been lost (e.g., Kok & Tauxe, 1999; Yamamoto et al., 2007). It is, however, necessary to seek potential for utilizing such sediments in order to obtain paleomagnetic records of higher time resolution or older ages; reductive diagenesis is usually progressed in sediments with a high sedimentation rate, which usually have a large input of organic matter, or in sediments buried deeply. In this study, we first document in detail compositional changes of magnetic mineral assemblages in sediments associated with reductive dissolution of magnetic minerals. Next, we examine contributions of individual magnetic components to remanent magnetization of the sediments. We show potential of relict hematite for paleomagnetic recording in sediments with reductive diagenesis. We then attempt RPI estimations to investigate the possibility of recovering meaningful paleomagnetic signals from diagenetically reduced sediments.

2. Geological Setting and Studied Material

Piston core MR1402-PC3 of 15.16 m long obtained from the Ontong Java Plateau (OJP) in the western equatorial Pacific Ocean during the R/V *Mirai* MR14-02 cruise in 2014 was used in this study (Figure 1). The coring site is at 0°12.00′S, 155°58.00′E with a water depth of 1923 m, which is above the present carbonate compensation depth of about 5250 m in this region (Valencia, 1973). The major lithology of the core is light gray to light olive-gray calcareous ooze (Figure S1 in Supporting Information S1). The uppermost ~5.1 m of the sediments suffered physical disturbance due to inner tube deformation during coring, but original stratigraphy appears to be preserved. A sediment color change from brown to light gray at ~20 cm in depth is recognized visually as the iron-redox boundary. The occurrence of the iron-redox boundary here is further confirmed by core color reflectance variations measured on board at 2 cm intervals (Figure S1 in Supporting Information S1).

The age model of core MR1402-PC3 was established by inter-core correlation with core MR1402-PC4 using color reflectance L* data (Figure S2 in Supporting Information S1). The latter core was taken from the OJP about

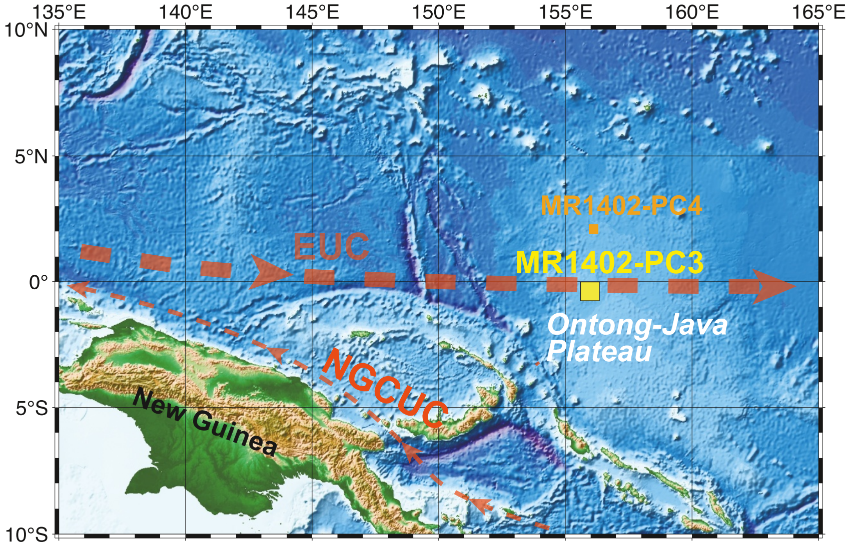

Figure 1. Topography of the western equatorial Pacific Ocean around the Ontong Java Plateau (OJP), and the locations of core MR1402-PC3 studied in this paper and core MR1402-PC4 referred in the text. Red arrows indicate the Equatorial Undercurrent (EUC) and New Guinea Coastal Undercurrent (NGCUC), which transport detrital materials from New Guinea to the OJP (Dang et al., 2020). This map was generated using Generic Mapping Tools software (Wessel et al., 2019).

250 km north of the former (Figure 1), and its age model was constructed based on $\delta^{18}O$ stratigraphy (Li Jiaxi et al., 2022). The average sedimentation rate of core MR1402-PC3 is approximately 1.4 cm/kyr, which is almost the same as that of core MR1402-PC4 (Li Jiaxi et al., 2022). The results of rock- and paleomagnetic study of core MR1402-PC4 were presented in Li Jiaxi et al. (2022), which was mainly aimed to clarify the influence on RPI estimation of changing proportion of magnetofossils to detrital magnetic minerals.

Discrete samples for rock- and paleomagnetic measurements were taken continuously on board from split core surfaces using open-ended plastic cubes of 7 cm^3 each. Immediately after collection, the samples were sealed tightly to prevent dehydration.

3. Method

3.1. Magnetic Susceptibility and Remanent Magnetization

Magnetic susceptibility was measured for all discrete samples using a Kappabridge KLY-4S susceptometer at Marine Core Research Institute (MaCRI), Kochi University. Natural remanent magnetization (NRM) was measured and subjected to a stepwise alternating-field (AF) demagnetization at peak fields of 5, 10, 15, 20, 25, 30, 35, 40, 50, 60, and 80 mT. The measurements were conducted on alternate samples throughout the sediment core using a pass-through cryogenic magnetometer (2G Enterprises Model 760R) at MaCRI with a noise level of $\sim 10^{-11}$ Am^2. Characteristic remanent magnetization (ChRM) component was determined by applying principal component analysis (PCA) (Kirschvink, 1980) to the NRM demagnetization data. The interval of demagnetization steps that minimize the maximum angular deviation (MAD) was selected for each sample on the condition of five or more consecutive steps. The fitting was not anchored to the origin. Subsequent to AF demagnetization of NRM, anhysteretic remanent magnetization (ARM) was imparted applying a 0.1 mT direct current (DC) field, which was superimposed to decaying AF with a peak field of 80 mT. The ARM was then subjected to stepwise AF demagnetization at the same AF steps as those in the case of NRM but excluding 5 mT. Next, isothermal remanent magnetization (IRM) was given by a 2.5 T DC field using a pulse magnetizer (Magnetic Measurements MMPM10) at MaCRI, which is regarded here as saturation IRM (SIRM). The SIRM was AF demagnetized at 20 mT for every fifth sample using a tumbling AF demagnetizer (Natsuhara-Giken D-spin) at Atmosphere and Ocean Research Institute (AORI), The University of Tokyo. To determine S-ratios, IRMs of 0.1 T and 0.3 T were successively imparted in the direction opposite to the initial IRM. The definition of Bloemendal et al. (1993) was used for the calculation of S-ratios ($S_{-0.1T}$ and $S_{-0.3T}$).

3.2. Rock Magnetism

To characterize magnetic mineral assemblages in the sediments, a suite of rock magnetic measurements was conducted, which includes low-temperature measurements, first-order reversal curve (FORC) measurements, IRM component analysis, thermal demagnetization of three-component IRM, and transmission electron microscopy (TEM). Refer Text S1 in Supporting Information S1 for the methodology.

3.3. Chemical Treatment and Magnetic Extraction

In the rock-magnetic measurements mentioned above, chemically treated and/or magnetically extracted samples were used in addition to untreated genuine samples. The purposes of the chemical treatments are (a) to dissolve carbonates to enhance magnetic concentration, and (b) to separate the contribution of silicate-hosted magnetic inclusions.

3.3.1. Acetic Acid Treatment

To better capture weak magnetic signals of the carbonate-rich sediments, acetic acid treatment was applied to selected samples to dissolve carbonates without affecting magnetic minerals. Freeze-dried samples were treated with buffered acetic acid (2 M, pH 4.5) for 72 hr (Hounslow & Maher, 1996; Thomas-Keprta et al., 2000). The samples were then washed with purified water and freeze-dried again.

3.3.2. Extraction of Silicate-Hosted Magnetic Inclusions

To estimate the concentration of silicate-hosted magnetic inclusions in the studied sediments, and to evaluate their contribution to remanent magnetization, quartz and feldspar were extracted from selected samples with sodium pyrosulfate ($Na_2S_2O_7$) fusion technique (Blatt et al., 1982; Clayton et al., 1972; Stevens, 1991; Syers et al., 1968). For detailed procedures, refer Usui et al. (2018) and Li Jiaxi et al. (2022). Any magnetic minerals that remain in the residues after the treatment should be magnetic-mineral inclusions in quartz and feldspar. The contribution of silicate-hosted magnetic inclusions to remanent magnetization was estimated by comparing SIRM before and after the chemical treatment (i.e., SIRM fraction). SIRM was imparted using a pulse magnetizer at a 2.7 T field and was measured using a spinner magnetometer at AORI.

3.3.3. Magnetic Extraction

To collect magnetic grains from the acetic acid-treated samples and the sodium pyrosulfate fusion residues, the samples were first dispersed in distilled water in an ultrasonic bath for about 5 min. Sodium hexametaphosphate was used as a deflocculant for the suspension. Magnetic grains were extracted from the suspension using a bottle with a high magnetic field gradient produced by a strong magnet (a magnetic finger, Kirschvink et al., 1992) without circulation. Finally, the magnetic extracts were dried or preserved in ethanol for further experiments.

3.4. Relative Paleointensity Estimation

For RPI estimations, both ARM and IRM were tested as normalizers to compensate for variations in sediment magnetizability (King et al., 1983; Tauxe, 1993). For preliminary assessment, NRM/ARM and NRM/IRM after blanket 20 mT AF demagnetization were adopted as RPI. Next, demagnetization diagrams between NRM-ARM pairs at corresponding AF demagnetization steps were constructed for each sample (modified version of the pseudo-Thellier plot of Tauxe et al. (1995)). To calculate RPI contributed by a particular magnetic component in a magnetic mineral assemblage, a coercivity window for calculating the best-fit slope on a NRM-ARM demagnetization diagram was determined based on the coercivity range of the magnetic component estimated using various rock-magnetic techniques including FORC diagram and IRM component analysis (Chen et al., 2017; Li Jiaxi et al., 2022; Ouyang et al., 2014; Yamazaki et al., 2023).

4. Results

4.1. Bulk Magnetic Properties

Magnetic susceptibility shows a gradual downcore decrease with large fluctuations in the upper part of the core, followed by a sudden drop at ~5.7 m in depth (Figure 2a). The gradual downcore decreasing trend above ~5.7 m

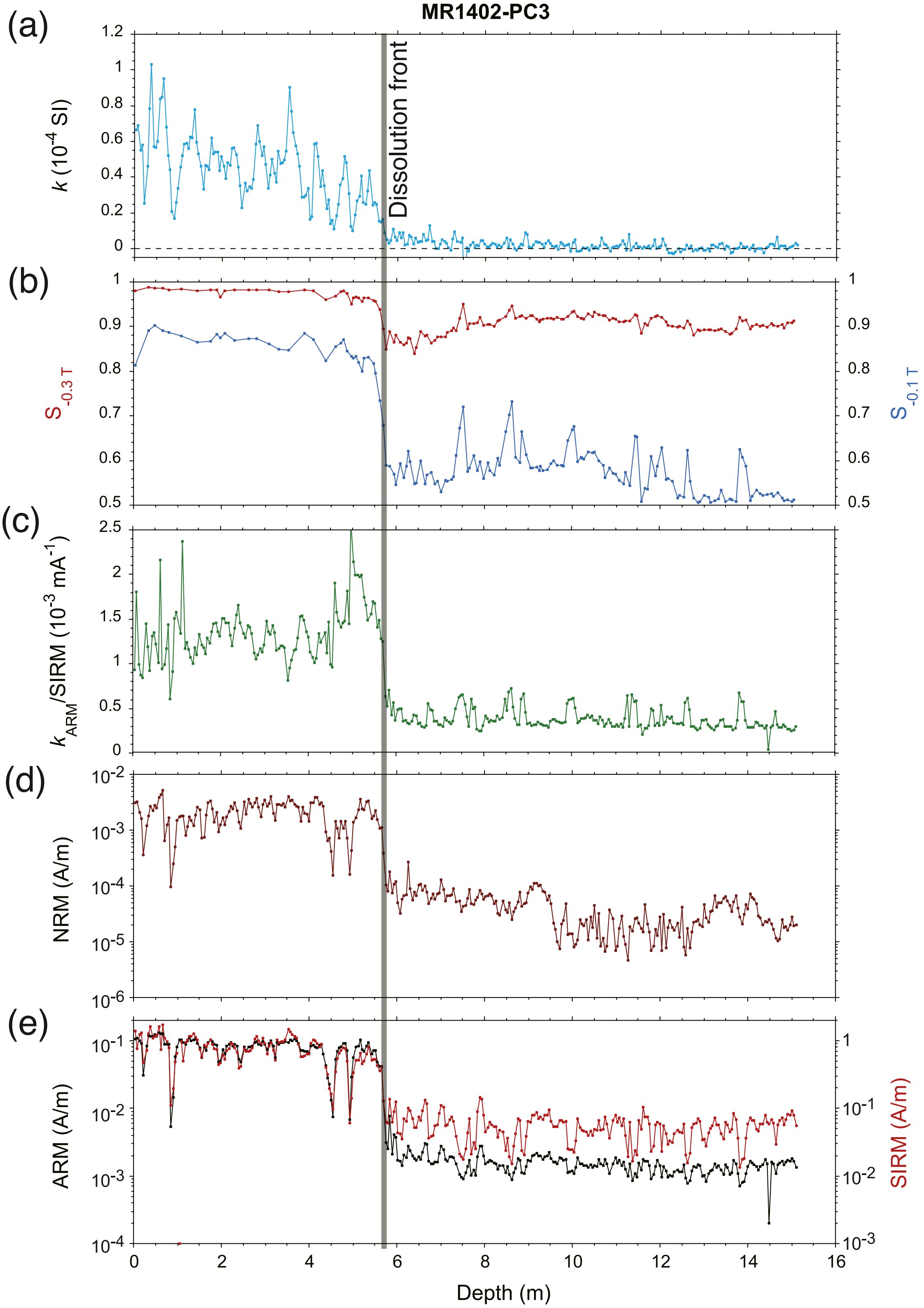

Figure 2. Variations of magnetic properties with depth of core MR1402-PC3. (a) Magnetic susceptibility (k), (b) S-ratios ($S_{-0.1T}$ in blue and $S_{-0.3T}$ in red), (c) the ratio of anhysteretic remanent magnetization (ARM) susceptibility (k_{ARM}) to saturation isothermal remanent magnetization (SIRM), (d) natural remanent magnetization (NRM) intensity, and (e) ARM (black) and SIRM (red) intensity. Gray line indicates the magnetite dissolution front.

is attributable to increasing dilution of magnetic minerals due to increasing carbonate content. Negative susceptibility values of some samples below ∼5.7 m indicate the dominance of diamagnetic carbonates. The sudden drop of the magnetic mineral concentration at ∼5.7 m is also evident from the coeval drops in NRM, IRM, and ARM (Figures 2d and 2e). Magnetization loss is 98%, 93%, and 98% in for NRM, IRM, and ARM, respectively. S-ratios show simultaneous drops, indicating increased magnetic coercivity of the mineral assemblages in average below ∼5.7 m (Figure 2b). The average $S_{-0.1\ T}$ decreases from 0.86 to 0.57, indicating that remanence is carried more by high-coercivity minerals below ∼5.7 m. These magnetic property changes across ∼5.7 m are due to reductive dissolution of magnetite (Roberts, 2015; Rowan et al., 2009; Yamazaki et al., 2003), and the magnetite dissolution front is defined at 5.7 m here. A simultaneous drop in k_{ARM}/SIRM ratio (Figure 2c) indicates the dissolution of unprotected magnetofossil because k_{ARM}/SIRM ratio is a proxy for relative abundance of magnetofossil in a magnetic mineral assemblage, particularly in pelagic environments (Egli, 2004; Yamazaki, 2008; Zhang et al., 2022).

4.2. Paleomagnetic Direction

Stepwise AF demagnetization of NRM revealed that NRM above the dissolution front is softer than that below in general (Figure S3a in Supporting Information S1). Above the dissolution front, ∼12% of the initial NRM in average remains after AF demagnetization at 80 mT, whereas ∼38% remains below. This suggests that NRM of the sediments suffered from reductive diagenesis is carried more by higher-coercivity magnetic minerals. Median destructive field (MDF) of ARM below the dissolution front at 5.7 m is higher than that above (Figure S3b in Supporting Information S1), which also indicates increased contribution of higher-coercivity magnetic minerals there. These observations are consistent with the concurrent drops in S-ratios (Figure 2b).

ChRM was extracted by applying PCA to NRM demagnetization data (Figure 3). The average MAD of the samples above the dissolution front is ∼5°, while that below is ∼23° (Figure 4b). The large MADs of the diagenetically reduced samples are partly due to very low NRM intensity, $\sim 1 \times 10^{-5}$ A/m or less, which leads to low signal-to-noise ratios on measurements at higher AF fields. In addition, AF demagnetization at a peak field of 80 mT is not sufficient to demagnetize high-coercivity remanence carriers, thus limiting the effective extraction of ChRM. Despite these limitations, meaningful ChRM directions were recovered from the diagenetically reduced sediments (Figure 4a). The selection of reliable direction data was based on demagnetization behavior of each sample, rather than applying a fixed MAD threshold. Accepted samples exhibit generally decreasing intensity with increasing AF field and have a linear segment on the demagnetization diagram (Figures 3d–3f). Samples exhibiting anomalous demagnetization behavior and/or lacking a linear segment were excluded (Figures 3g–3i). The Matuyama-Brunhes polarity transition is identified from a relative declination flip of about 180° at ∼787 ka. There is an age difference of ∼14 kyr compared to the recently proposed age of 773 ka for the Matuyama-Brunhes transition (Channell et al., 2020; Singer, 2014; Suganuma et al., 2015). As the average sedimentation rate of the core is approximately 1.4 cm/kyr, depositional remanent magnetization (DRM) depth-lag of ∼20 cm is estimated, which is similar to the case of nearby core MR1402-PC4 (Li Jiaxi et al., 2022). In addition, a short normal-polarity interval spanning from ∼975 to 1068 ka is considered to be a manifestation of the Jaramillo subchron (Figure 4a).

4.3. Magnetization of Silicate-Hosted Magnetic Inclusions and Grain Size of Host Silicates

Mass fraction of sodium pyrosulfate fusion residues is ∼2.3% of the untreated sediment samples, which shows no apparent downcore variation (Table 1). On the other hand, SIRM fraction of silicate-hosted magnetic inclusions exhibits a substantial downcore increase across the dissolution front at 5.7 m, from average values of 10.7% above to 54.9% below (Table 1). Thus, silicate-hosted magnetic inclusions are a minor detrital magnetic component above the dissolution front, whereas they are the major component below.

Mass-normalized SIRM of the grains magnetically extracted from the fusion residues is $\sim 5.17 \times 10^{-2}$ Am^2/kg in average (Table 1). As the ratio of saturation remanent magnetization to saturation magnetization (M_r/M_s) of the fusion residues is determined to be 0.219 ± 0.040 ($n = 8$) from magnetic hysteresis measurement (Table 1), saturation magnetization of the fusion residues is calculated to be ∼0.235 Am^2/kg. Assuming that the magnetic inclusions are magnetite, the concentration is estimated to be ∼0.25 wt. % from its saturation magnetization of 92 Am^2/kg (O'Reilly, 1984).

Grain sizes of the fusion residues above and below the dissolution front show similar unimodal distributions (Figure S4 in Supporting Information S1). The median diameter is ∼11 μm, and approximately 75% of grains fall

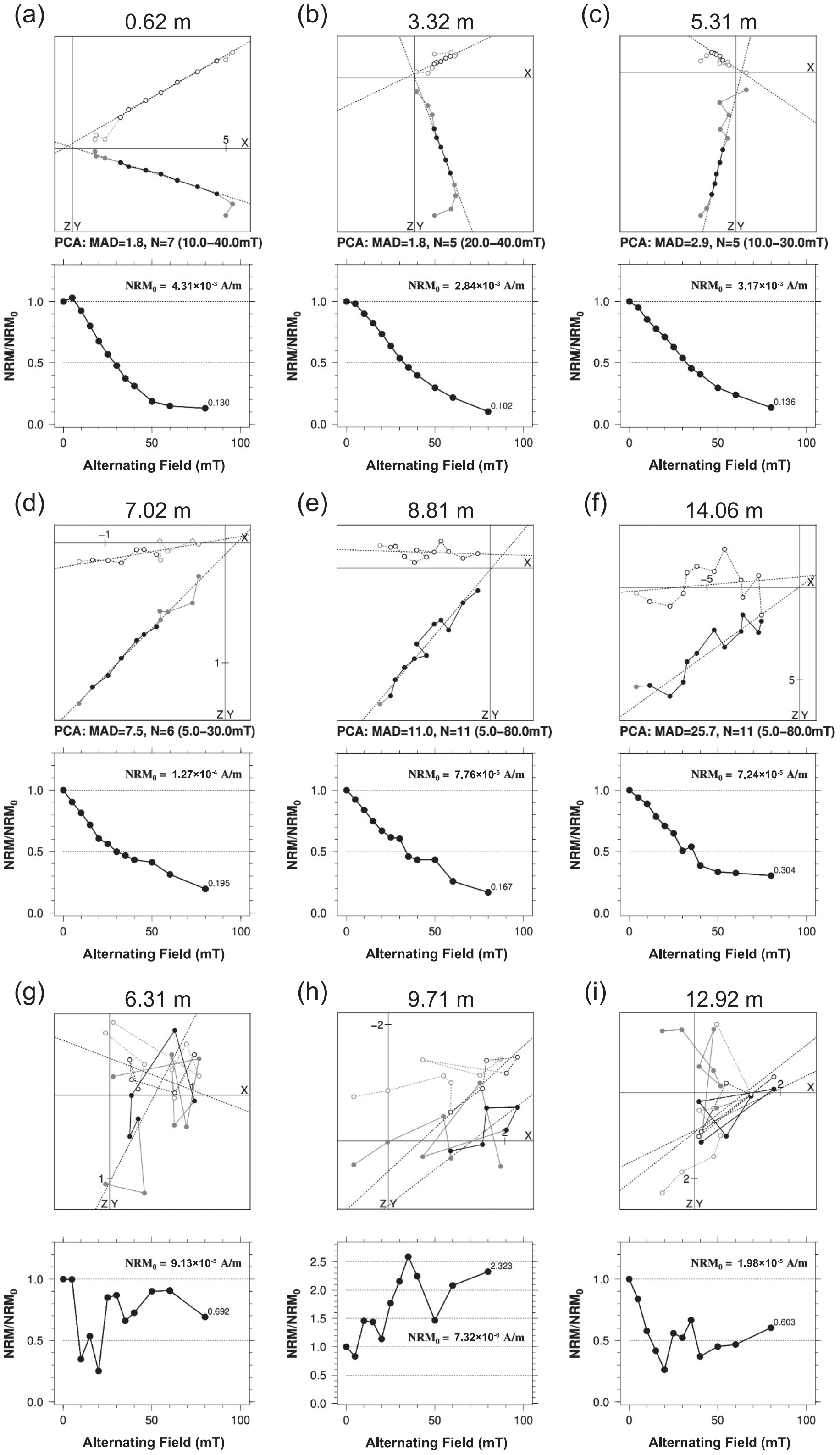

Figure 3. Examples of stepwise alternating-field demagnetization of natural remanent magnetization (NRM) for accepted samples above the dissolution front (a–c) and accepted (d–f) and excluded samples (g–i) below the dissolution front. Solid (open) symbols are horizontal (vertical) projection of vector end points. N: number of demagnetization steps used for principal component analysis, MAD: maximum angular dispersion.

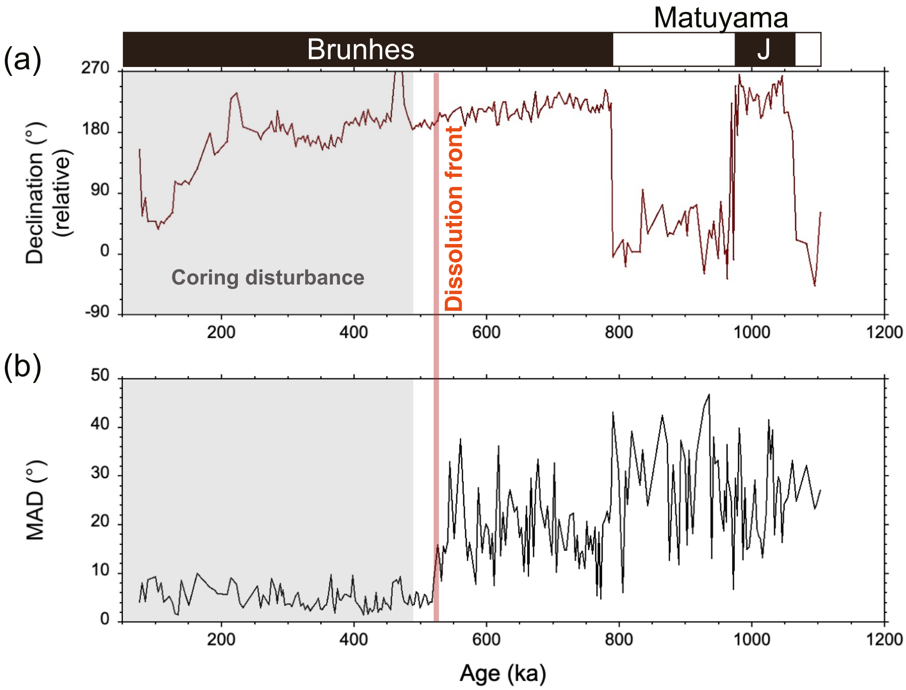

Figure 4. Relative declination (a) and maximum angular deviation of principal component analysis (MAD) (b) of core MR1402-PC3. Magnetic polarity interpretation is shown on the top. J: Jaramillo subchron. Orange line indicates the magnetite dissolution front. Shaded interval may be influenced by coring disturbance.

in the range of 5–20 μm in diameter. The concentration of magnetic inclusions and the size and morphology of host silicates are key parameters to assess DRM acquisition efficiency of silicate-hosted magnetic inclusions, which will be discussed later.

4.4. Low-Temperature Measurement

Above the dissolution front at 5.7 m, a decrease of magnetization at ~100 K is pronounced in zero-field SIRM warming curves, which is indicative of the Verwey transition of magnetite (Verwey, 1939) (red curves in Figure 5b). Derivative curves (black curves in Figure 5b) revealed broad bell-shaped peaks at ~100–120 K. These

Table 1
Physical Properties of Core MR1402-PC3 Samples Before and After Chemical Extraction of Quartz and Feldspar

Depth (m)	Age (ka)	SIRM untreated (10^{-6}Am^2)	SIRM residues (10^{-6}Am^2)	Magnetization fraction residues (%)	Mass fraction residues (%)	Mass-normalized SIRM untreated (10^{-3}Am^2/kg)	Mass-normalized SIRM residues (10^{-3}Am^2/kg)	Mass-normalized SIRM magnetically extracted residue (10^{-3}Am^2/kg)	*Mr/Ms* residues
0.67	134	8.36	0.34	4.11	2.04	2.36	4.74	–	0.222
1.99	279	3.33	0.29	8.58	2.76	0.71	2.21	–	0.175
3.53	385	8.53	1.39	16.28	5.10	2.34	7.48	78.83	0.149
5.07	484	4.07	0.56	13.84	2.65	0.88	4.60	49.01	0.241
7.30	632	0.33	0.18	54.84	1.91	0.09	2.55	–	0.274
8.28	707	0.34	0.12	34.61	1.57	0.10	2.16	–	0.239
9.26	768	0.53	0.33	61.59	2.20	0.10	2.93	–	0.223
10.20	820	0.32	0.21	65.66	2.19	0.06	1.81	41.54	0.231
11.26	893	0.09	0.05	49.85	2.12	0.03	0.61	–	–
12.94	968	0.21	0.12	60.59	1.57	0.05	2.03	37.23	–
14.66	1076	0.13	0.07	56.96	1.68	0.04	1.50	–	–

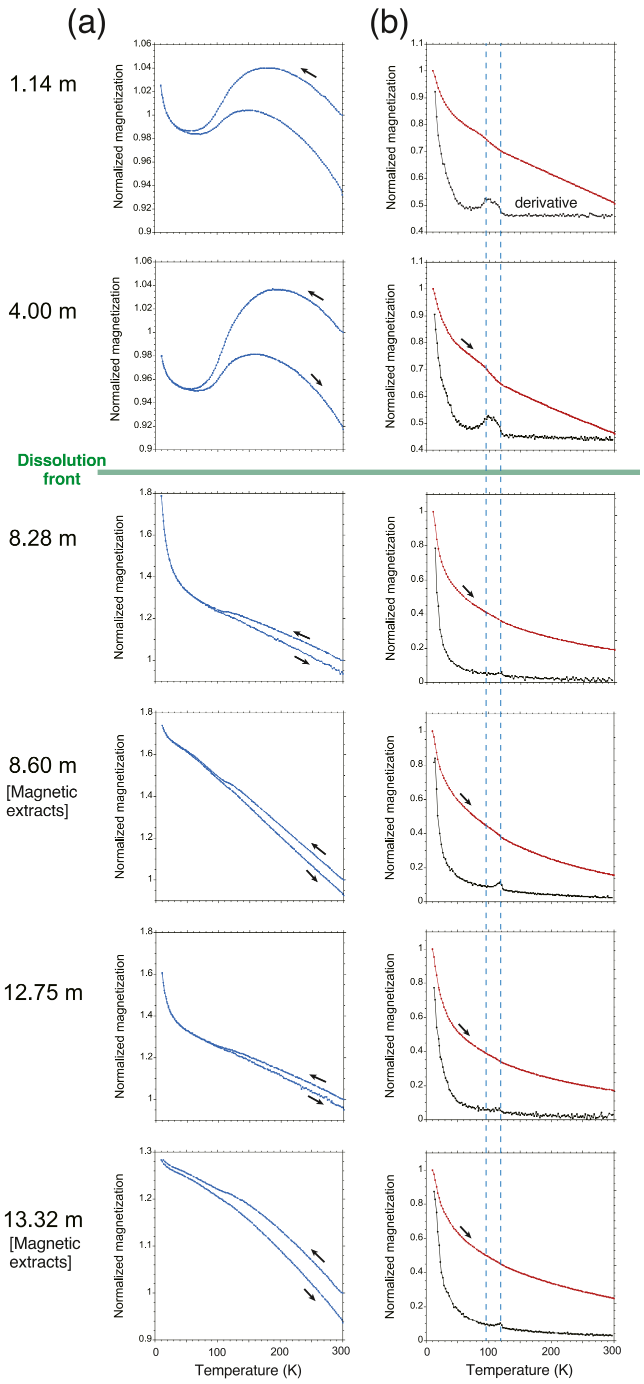

Figure 5. Results of low-temperature magnetic measurements. (a) Low-temperature cycling of isothermal remanent magnetization (IRM) acquired at 300 K in a 3 T field normalized by IRM at 300 K, and (b) thermal decay curve of IRM imparted at 10 K in a 3 T field normalized by IRM at 10 K (red), with derivative of the curve (black). Blue dashed lines show empirical Verwey transition temperatures of biogenic magnetite (~100 K) and stoichiometric inorganic magnetite (~120 K) (Chang, Heslop, et al., 2016). Samples at 8.60 and 13.32 m are magnetic extracts, whereas others are untreated.

observations indicate that magnetic minerals in the sediments above the dissolution front are a mixture of magnetofossil and inorganic stoichiometric magnetite (Chang, Heslop, et al., 2016; Li Jinhua et al., 2009; Pan et al., 2005). Below the dissolution front, the Verwey transition signals are barely recognized. The zero-field SIRM warming measurements were also conducted on magnetic extracts from 8.6 and 13.32 m. Derivative curves show a peak at ~120 K. These observations indicate that magnetofossil was dissolved and only part of unprotected detrital magnetite survived diagenetic dissolution.

In low temperature cycling measurements, samples above the dissolution front show significant irreversible remanence loss in a temperature range between ~100 and 300 K (Figure 5a), indicative of the occurrence of magnetite. Below the dissolution front, magnetization monotonically increases during cooling, and irreversible remanence loss during warming is small (Figure 5a). The magnetite signal may be overwhelmed by a paramagnetic signal induced by a small residual field inside the magnetometer, which is supported by the observation that magnetic extracts show little increase of magnetization in a temperature range below ~30 K whereas untreated samples show a large increase.

4.5. FORC Diagram

FORC diagrams above the dissolution front at 5.7 m show a sharp central ridge along $B_u = 0$ with a peak B_c at ~25 mT and a broad component with wide B_u distributions (Figures 6a–6d). This indicates that magnetic minerals in the sediments comprise a mixture of magnetofossil and detrital magnetite ranging from the single-domain (SD) to vortex states (Chang et al., 2014; Inoue et al., 2021; Roberts et al., 2014; Yamazaki, 2008; Yamazaki et al., 2020). The FORC distribution pattern of these samples is similar to that of nearby core MR1402-PC4 (Li Jiaxi et al., 2022), indicating similar magnetic mineral compositions between the two cores.

Below the dissolution front, on the other hand, the central ridge signature is obscure, and the coercivity of a FORC distribution peak becomes lower (Figures 6e–6h). This can be explained by reductive dissolution of magnetofossil and finer unprotected detrital magnetite (Roberts et al., 2018). This interpretation is consistent with the results of the low-temperature measurements mentioned above and the drop of k_{ARM}/SIRM (Figure 2c). In addition, FORC distributions near the origin of the diagram are more pronounced compared with that above the dissolution front, which suggests the presence of superparamagnetic (SP) grains in the reduced sediments.

FORC diagrams of sodium pyrosulfate fusion residues revealed magnetic properties of silicate-hosted magnetic inclusions (Figures 6i–6p). A central ridge-like signal with wider vertical spread of the inner contours compared with the central ridge of magnetofossil origin indicates the presence of weakly interacting SD grains in silicates (Egli, 2006; Inoue et al., 2021). Diverging outer contours of the FORC distribution indicate the presence of vortex-state magnetic inclusions. Continuous FORC distributions along the B_c axis from the origin indicate the presence of inclusions with SP and near SP/SD boundary sizes. The FORC distribution pattern of the silicate-hosted magnetic inclusions in the studied sediments is similar to that of nearby core MR1402-PC4 (Li Jiaxi et al., 2022) and a core from the West Caroline Basin about 2300 km west of the present core (Inoue et al., 2021), suggesting a common provenance of the detrital grains, likely transported from New Guinea (Figure 1).

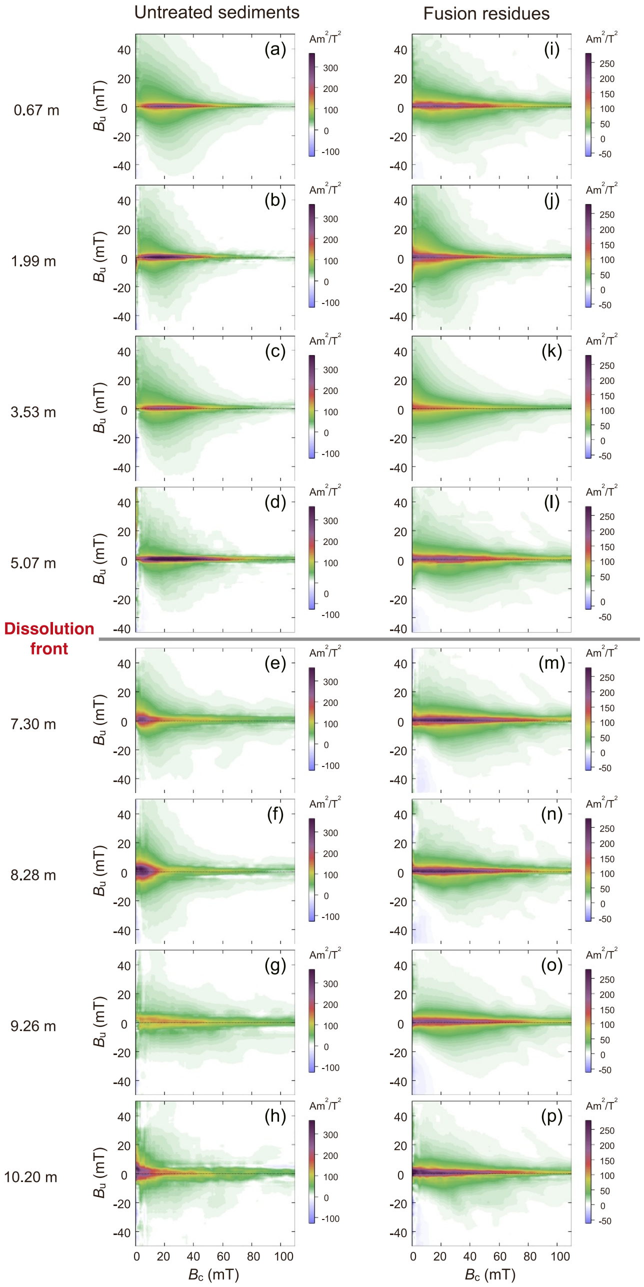

Figure 6. First-order reversal curve (FORC) diagrams for untreated samples (a–h) and sodium pyrosulfate fusion residues (silicate-hosted magnetic inclusions) (i–p). The upper four rows are samples above the dissolution front, and the lower four rows are samples below it. Smoothing factors (SFs) applied to the untreated samples above the dissolution front (a–d) are $S_{c0} = 4$, $S_{b0} = 3$, $S_{c1} = S_{b1} = 7$, and $\lambda_c = \lambda_b = 0.1$ whereas below the dissolution front (e–h) are $S_{c0} = 6$, $S_{b0} = 4$, $S_{c1} = S_{b1} = 12$, and $\lambda_c = \lambda_b = 0.1$. SFs applied for the fusion residues (i–p) are $S_{c0} = 4.5$, $S_{b0} = 3$, $S_{c1} = S_{b1} = 8$, and $\lambda_c = \lambda_b = 0.1$.

4.6. IRM Component Analysis

Supervised IRM decomposition was applied in this study to mitigate inherent non-uniqueness of IRM decomposition, which incorporates a priori information obtained from independent rock-magnetic analyses as constraints (Heslop, 2015). Coercivity distribution and dispersion parameter (DP) of silicate-hosted magnetic inclusions were first determined from IRM acquisition curves of sodium pyrosulfate fusion residues (Figure 7h). A predominant component with a mean coercivity of ~65 mT and a DP of ~0.37 was identified as representing the silicate-hosted magnetic inclusions (hereafter component C1). This result is consistent with the coercivity distribution of the central ridge-like FORC signatures of the fusion residues (Figure 6o). The parameters of C1 were then used as a priori information in the IRM component analyses of chemically untreated samples.

Above the dissolution front at 5.7 m, remanence is carried mainly by two components (Figures 7a–7c, Table 2). C2 has a mean coercivity of ~26 mT and a DP of 0.37–0.39, which carries ~53% of the remanence. C5 has a mean coercivity of ~51 mT and a DP of 0.26–0.28, which carries ~35% of the remanence. Based on the rock-magnetic evidence obtained from low-temperature measurements and FORC diagrams, C2 and C5 are interpreted to represent detrital magnetite and magnetofossil, respectively. C1 (silicate-hosted magnetic inclusions) carries ~7% of the remanence. Other two minor components are identified, C3 with a mean coercivity of ~231 mT and C4 with much higher coercivity.

In the samples below the dissolution front, remanence is carried mainly by C1 and C3, which explain 46%–63% and 21%–34% of the remanence, respectively (Figures 7d–7g, Table 2). C5 no longer exists, indicating loss of magnetofossil by reductive dissolution. C2 contributes less to the remanence with a lower coercivity, and has a larger DP compared with those above the dissolution front. These changes in C2 can be explained by partial dissolution of unprotected detrital magnetite; finer grains were lost earlier due to their higher surface-to-volume ratio, whereas coarser grains partly survive. C3 is interpreted to be carried by hematite considering its resistivity against reductive dissolution (Abrajevitch et al., 2009; Abrajevitch & Kodama, 2011; Yamazaki et al., 2003). The presence of hematite is further supported by thermal demagnetization of three-component IRM (Text S2, Figures S5 and S6 in Supporting Information S1). C4 likely represents goethite (Roberts, 2015; Roberts, Florindo et al., 2013).

Downcore variations in SIRM fractions of unprotected magnetic minerals, silicate-hosted magnetic inclusions, and hematite are presented in Figure 8 as a summary of the IRM component analyses.

4.7. TEM Observation

TEM observations were conducted on magnetic extracts from a chemically untreated sample at 1.14 m (Figures 9a–9c), an acetic acid-treated sample at 6.17 m (Figures 9d–9f), and sodium pyrosulfate fusion residues at 7.3 m (Figures 9g–9i). Obtained TEM images support the interpretations of the rock-magnetic measurements mentioned above.

Above the dissolution front at 5.7 m, abundant magnetofossils are identified from distinct morphologies (e.g., octahedral, hexagonal prism, and bullet-shaped) and SD grain size (Akai et al., 1991; Bazylinski et al., 1994; Li Jinhua et al., 2020; Yamazaki et al., 2019) (Figures 9a–9c). Fine-grained detrital magnetic minerals are also recognized as irregularly shaped particles alongside magnetofossils. In the sample just below the dissolution

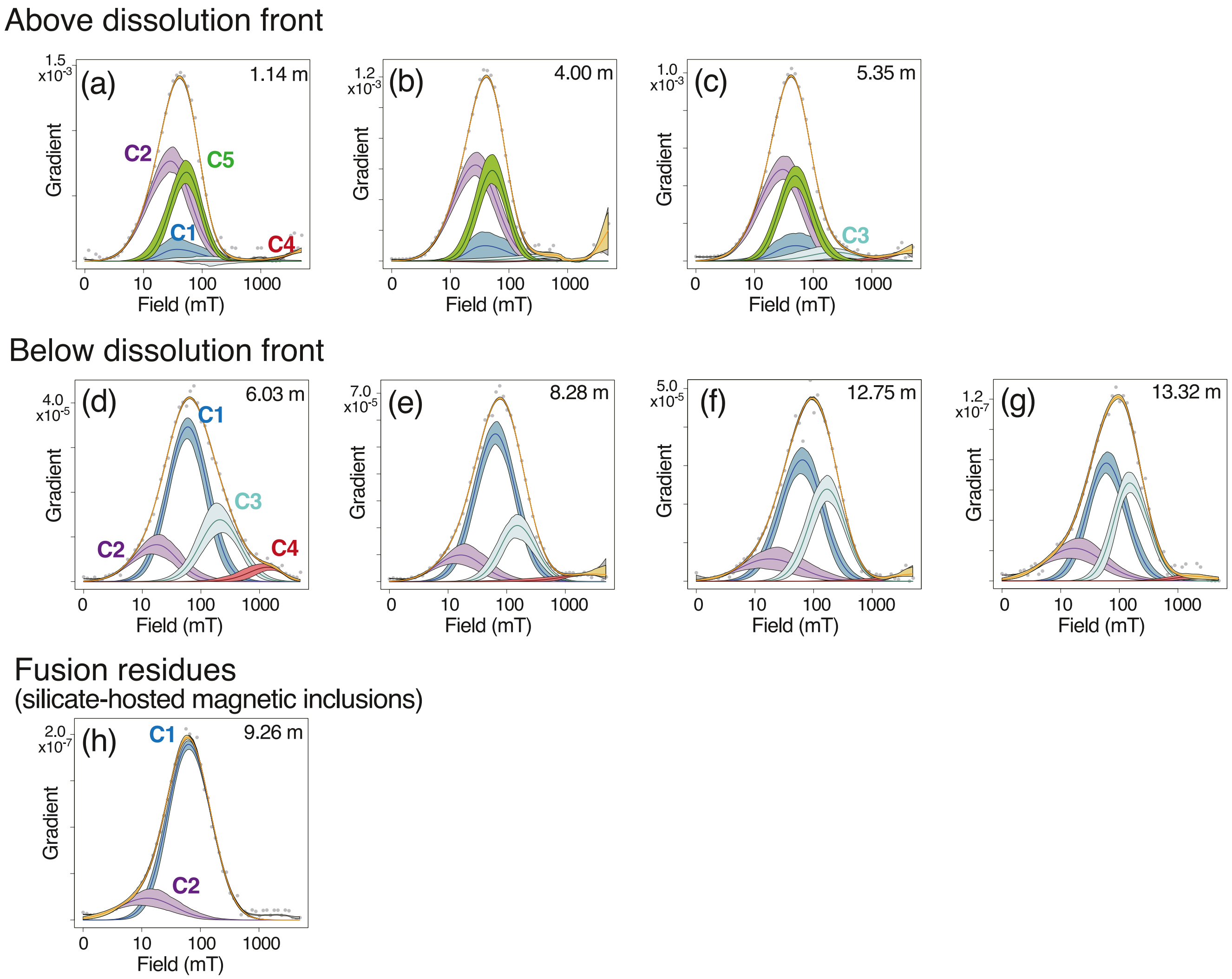

Figure 7. Isothermal remanent magnetization (IRM) decomposition results of samples above the dissolution front (a–c), below the dissolution front (d–g), and sodium pyrosulfate fusion residues (silicate-hosted magnetic inclusions) (h). The observed data (gray circles) are fitted by the sum (yellow curve) of five components with 95% confidence intervals. First, the data of silicate-hosted magnetic inclusions were analyzed, and resulting components C1 (blue) and C2 (purple) were used as a priori information for fitting of other untreated samples. Components C2 (purple) and C5 (green) are dominant in samples above the dissolution front, whereas C1 (blue) and C3 (cyan) are dominant below the dissolution front. A minor high-coercivity component C4 (red) is introduced for optimal fit.

front, detrital magnetic minerals in vortex-state sizes are abundant (Figures 9d–9f). Partially dissolved magnetofossils indicated by etched edges and wavy corrosion (Yamazaki, 2020) are occasionally observed at this depth (arrows in Figure 9f). Silicate-hosted magnetic inclusions are recognized in the fusion residues based on their distinct microstructures, where dark fine grains are embedded in transparent host minerals (Figures 9g–9i). The magnetic inclusions have grain sizes ranging from SP to the vortex state. These observations are consistent with the FORC diagrams of fusion residues (Figures 6i–6p). Magnetic inclusions appear mainly as subrounded particles randomly distributed within host silicates with no specific crystallographic orientation. Host silicates have irregular shapes with diameters ranging from hundreds of nanometers to several microns without strong elongation.

4.8. Relative Paleointensity Estimation

Substantial diagenetic alteration in magnetic mineral assemblages of core MR1402-PC3 does not satisfy the prerequisite of reliable RPI estimations, that is, uniformity of magnetic mineralogy (Tauxe, 1993). A large magnetic mineral concentration change across the dissolution front does not meet the criteria of reliable RPI estimations either. Thus, this core is not favorable for reliable RPI estimations. The purpose of RPI estimation

Table 2
Summary of IRM Component Analysis

	Component 1			Component 2			Component 3			Component 4			Component 5		
Depth (m)	Bh (mT)	DP	C (%)	Bh (mT)	DP	C (%)	Bh (mT)	DP	C (%)	Bh (T)	DP	C (%)	Bh (mT)	DP	C (%)
1.14	49	0.33	5.93	26	0.37	55.5	223	0.43	1.13	12.6	0.42	2.12	51	0.27	35.4
4.00	47	0.34	7.39	25	0.37	52.2	248	0.39	2.76	8.90	0.30	3.21	51	0.26	34.4
5.35	56	0.36	7.87	28	0.39	50.6	223	0.41	5.19	7.99	0.45	2.59	50	0.28	33.8
6.03	59	0.34	57.2	16	0.38	15.4	210	0.34	22.8	1.15	0.29	4.56	–	–	–
8.28	63	0.35	63.4	16	0.39	12.8	158	0.30	20.7	3.23	0.53	3.18	–	–	–
9.26	65	0.37	86.3	12	0.48	13.7	–	–	–	–	–	–	–	–	–
12.75	60	0.36	51.7	18	0.50	13.1	168	0.31	33.6	6.74	0.48	1.57	–	–	–
13.32	62	0.33	45.8	17	0.50	18.8	165	0.29	33.8	2.11	0.36	1.61	–	–	–

Note. Bh: mean coercivity, DP: dispersion parameter, C: relative contribution.

here is to examine the influence of reductive diagenesis on RPI. The intervals above and below the dissolution front are treated separately. It should also be noted that above ~5.5 m (~490 ka) reliable RPI estimations are hampered by some physical disturbance of the core.

For preliminary RPI estimations, NRM after AF demagnetization at 20 mT was normalized by ARM and IRM after AF demagnetization at 20 mT (hereafter NRM/ARM_20 mT and NRM/IRM_20 mT) (Figure 10a and red curve in Figure 10b). The samples from which a ChRM component could not be extracted were excluded from RPI estimations. As k_{ARM}/SIRM drops across the dissolution front (Figure 2c), RPIs of ARM and IRM normalizations are expected to be significantly different. NRM/ARM_20 mT (red curve in Figure 10b) does not show a large change across the dissolution front and has general agreement with the PISO-1500 paleointensity stack (Channell et al., 2009) (Figure 10c). The correlation coefficient is 0.36 after slight adjustment of age shown by the tie-lines in Figure 10c. On the other hand, NRM/IRM_20 mT exhibits attenuated intensities below the dissolution front (Figure 10a). This implies that IRM overestimates DRM acquisition efficiency of relict magnetic minerals, and hence NRM/IRM_20 mT underestimates RPI.

To extract RPI signals of individual magnetic components identified by the IRM component analysis, RPIs were calculated from the best-fit slopes in specific coercivity windows on NRM-ARM demagnetization diagrams (Figure 11), following the idea of Chen et al. (2017), Li Jiaxi et al. (2022), Ouyang et al. (2014) and Yamazaki et al. (2023). Above the dissolution front, detrital magnetite and magnetofossil are recognized as the major remanence carriers. Varying proportions of magnetofossil can influence RPI estimations (Inoue et al., 2021; Li Jiaxi et al., 2022; Yamazaki et al., 2013). To mitigate this influence, RPI was calculated from the best-fit slope in a low-coercivity (10–25 mT) window (hereafter NRM/ARM_10–25 mT) on NRM-ARM demagnetization diagrams, which reflects mainly the detrital unprotected magnetite (C2 of the IRM component analysis) (Figures 11a–11c). Below the dissolution front, remanence is interpretated to be carried mainly by silicate-hosted

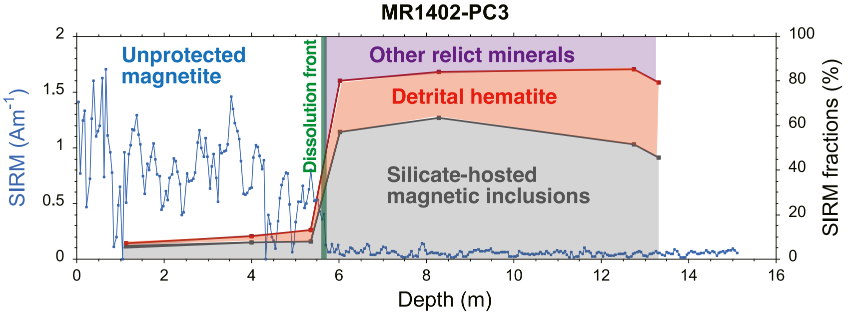

Figure 8. Saturation isothermal remanent magnetization (SIRM) (blue curve) of core MR1402-PC3 and fractions of SIRM carried by various magnetic components: unprotected magnetite (blue), silicate-hosted magnetic inclusions (gray), detrital hematite (red), and other relict minerals (purple). Green line indicates the magnetite dissolution front.

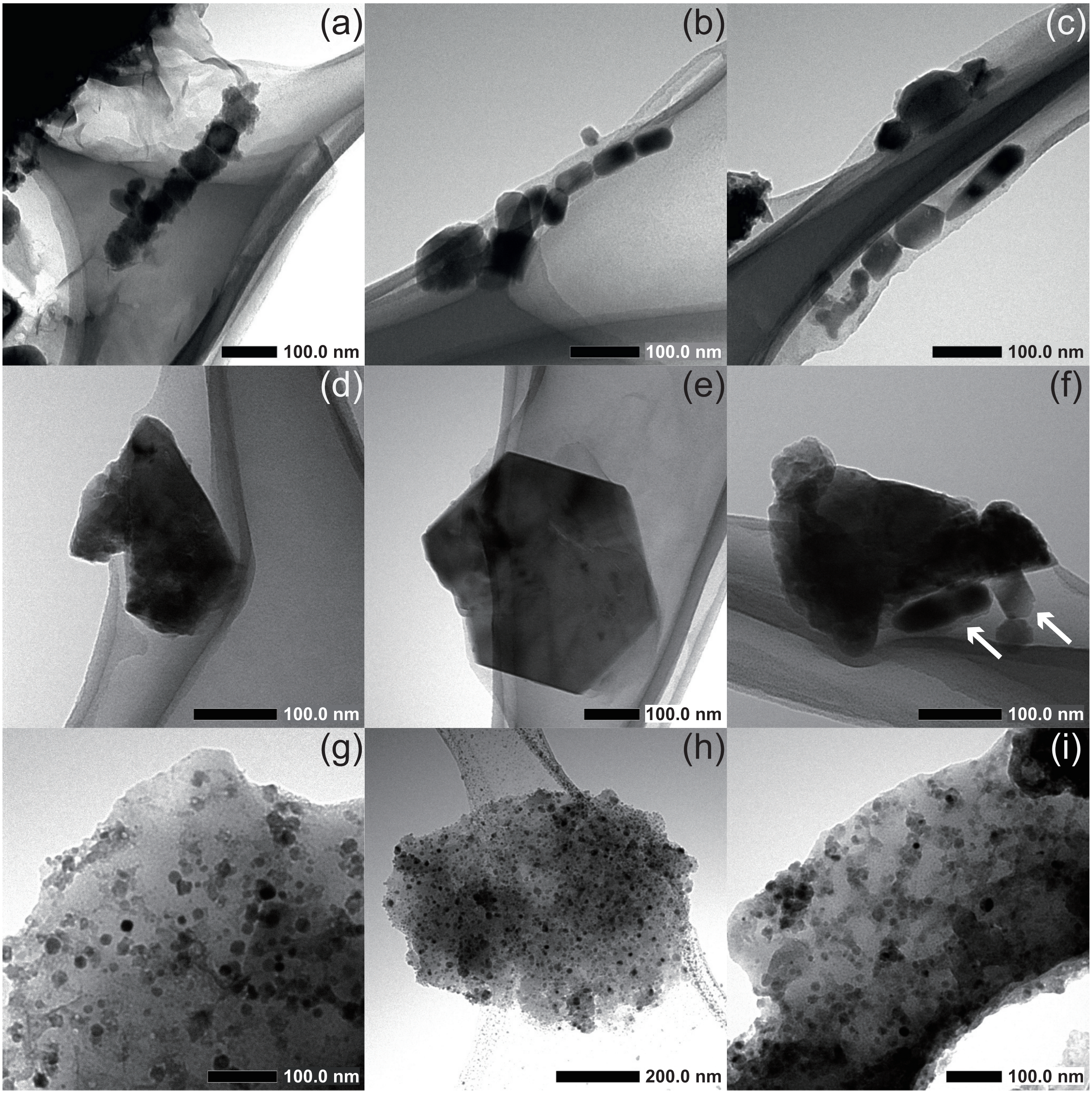

Figure 9. Transmission electron microscope (TEM) images of magnetic extracts from untreated sediments at 1.14 m (a–c), acetic acid-treated sediments at 6.17 m (d–f), and sodium pyrosulfate fusion residues at 7.3 m (g–i). Arrows indicate partial dissolution of magnetofossil.

magnetic inclusions and hematite with mean coercivities of ~62 and ~175 mT, respectively, from the IRM component analyses (Table 2). A higher-coercivity (25–50 mT) window was adopted for RPI calculation (hereafter NRM/ARM_25–50 mT), focusing on the coercivities of silicate-hosted magnetic inclusions (Figures 11d–11f). Contribution of hematite with relatively low coercivities, which is indicated by the left tail of the coercivity spectrum of the IRM component C3 (Figures 7d–7g), would also be included in this coercivity window. The RPI estimations may have been improved if AF demagnetization at a peak field of >80 mT and measurements with enhanced signal-to-noise ratios were possible. In summary, the overall agreement of the RPIs from the cores MR1402-PC3 (NRM/ARM_20 mT, NRM/ARM_10–25 mT, and NRM/ARM_25–50 mT)

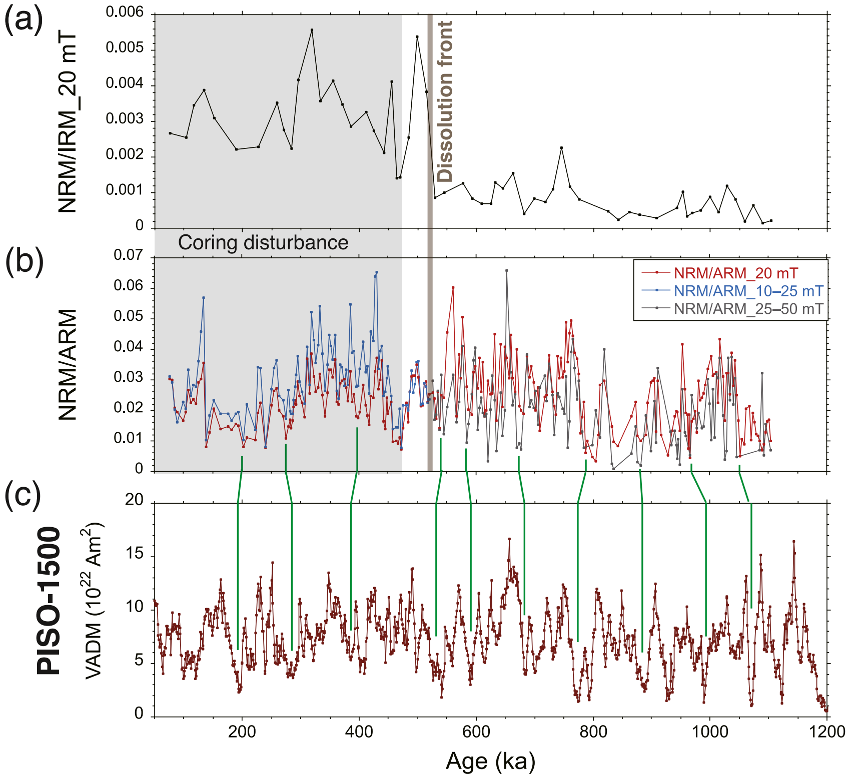

Figure 10. (a) Relative paleointensity (RPI) estimated from natural remanent magnetization (NRM) intensity normalized by isothermal remanent magnetization (IRM) intensity after blanket 20 mT alternating-field (AF) demagnetization, (b) RPI normalized by anhysteretic remanent magnetization (ARM): blanket AF demagnetization at 20 mT (red), and best-fit slope of NRM-ARM demagnetization diagram using a 10–25 mT window (blue) above the dissolution front (blown line) and a 25–50 mT window (gray) below it, and (c) the PISO-1500 paleointensity stack (Channell et al., 2009). Correlation with ARM-normalized RPI of MR1402-PC3 are indicated by green tie lines. VADM: virtual axial dipole moment. The interval shaded in gray in panels (a, b) may be influenced by coring disturbance.

(Figure 10b) and the PISO-1500 paleointensity stack (Figure 10c) highlights the possibility of recovering RPI from sediments subjected to reductive diagenesis.

5. Discussion

The magnetic constituents of core MR1402-PC3 sediments have been characterized by a series of rock-magnetic measurements and TEM observations described above. Above the dissolution front at 5.7 m, the major carriers of the remanent magnetization are unprotected detrital magnetite and magnetofossil. The average k_{ARM}/SIRM of ~1.35 mm/A above the dissolution front (Figure 2c) is comparable to that of magnetofossil-rich sediments reported previously (Usui & Yamazaki, 2021; Yamazaki et al., 2013; Yamazaki & Shimono, 2013; Zhang et al., 2022). Abundant magnetofossils and their substantial contribution to paleomagnetic records were reported in a number of paleomagnetic studies of sediments from the OJP (Li Jiaxi et al., 2022; Tarduno et al., 1998; Yamazaki, 2009; Yamazaki & Solheid, 2011). Below the dissolution front, unprotected detrital magnetite and magnetofossil dissolved, and two relict magnetic minerals, silicate-hosted magnetic inclusions and detrital hematite, carry the remanent magnetization (Figure 8). It is intriguing that meaningful paleomagnetic direction and RPI records are recovered even from such sediments (Figures 4 and 10).

5.1. Silicate-Hosted Magnetic Inclusions

Recently, it has become recognized that silicate-hosted magnetic inclusions of detrital origin are widespread in marine sediments, and their magnetic properties and contributions to paleomagnetic records were discussed (Chang et al., 2021; Chang, Roberts, et al., 2016; Chen et al., 2017; Hong et al., 2019). In this study, it was revealed that silicate-hosted magnetic inclusions are a dominant magnetic component below the dissolution front

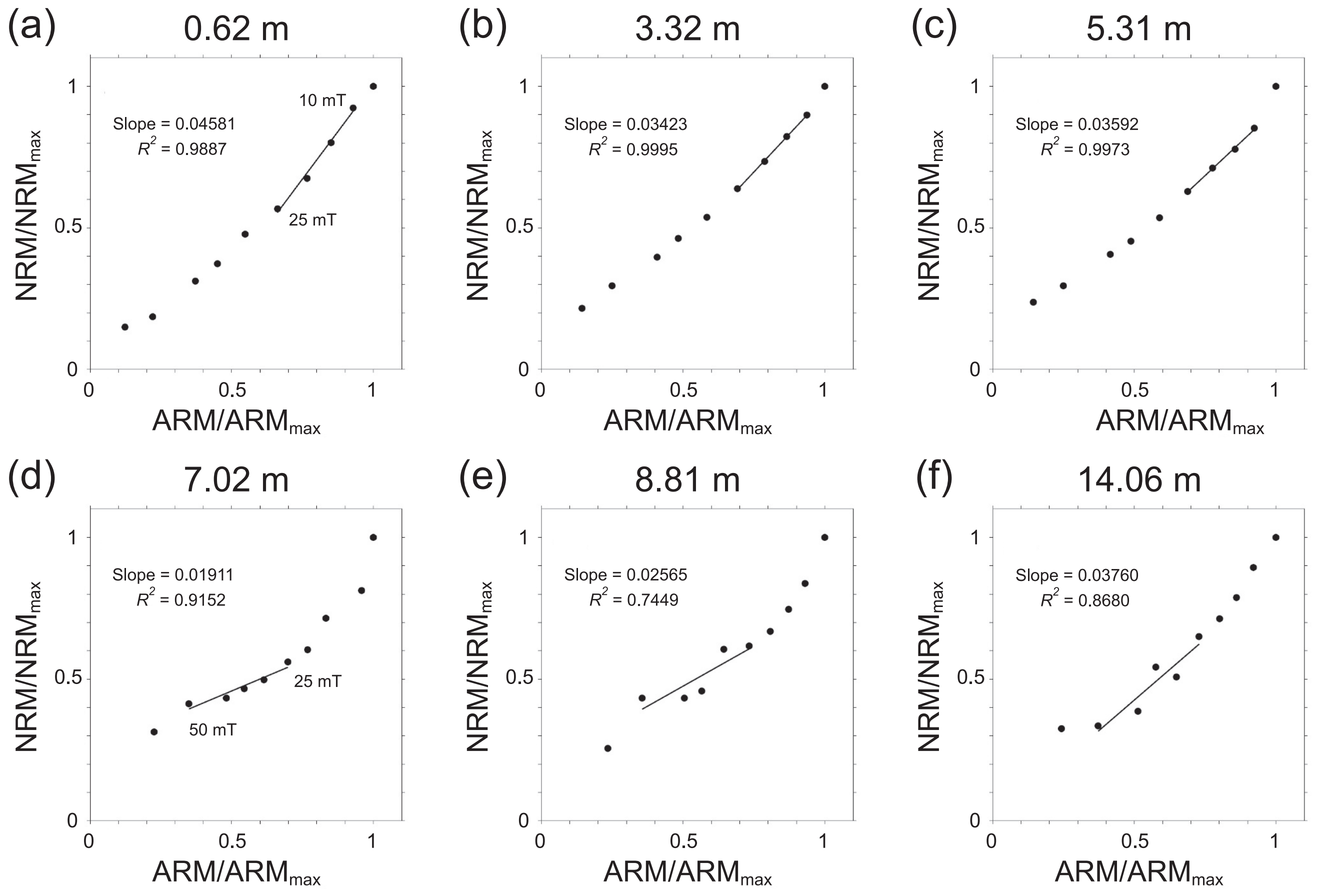

Figure 11. Examples of relative paleointensity (RPI) estimations from best-fit slopes on demagnetization diagrams of natural remanent magnetization (NRM) versus anhysteretic remanent magnetization (ARM) using a 10–25 mT window for samples above the dissolution front (a–c) and a 25–50 mT window below it (d–f).

from the large SIRM fraction carried by sodium pyrosulfate fusion residues and the IRM component analysis (Figure 8, Tables 1 and 2). These grains are likely of fluvial origin transported from the northern coast of New Guinea by the New Guinea Coastal Undercurrent and the Equatorial Under Current (Dang et al., 2020; Inoue et al., 2021) (Figure 1).

The large SIRM fraction of the silicate-hosted magnetic inclusions in the studied sediments does not necessarily mean a large contribution to the paleomagnetic record. DRM acquisition efficiency of the silicate-hosted magnetic inclusions in the studied sediments is roughly evaluated here based on the insights of Chang, Roberts et al. (2016). They developed a numerical model to depict competing relationship between magnetic aligning torque and hydrodynamic torque for host silicates with specific diameters and aspect ratios and magnetite concentration within them (Figure 12). Given the median diameter of 11 μm without strong elongation and the magnetite concentration of ∼0.25 wt. % as mentioned above, the silicate-hosted magnetic inclusions in our samples mainly lie in a domain where hydrodynamic torque dominates in Figure 12. Therefore, it is estimated that the silicate-hosted magnetic inclusions in the studied sediments possess relatively low DRM acquisition efficiency, and that only a fraction of the silicate grains having smaller diameters (note that approximately 30% of the fusion residues have diameters smaller than 8 μm as indicated by the grain size analyses) and/or higher magnetite concentrations like the grains in Figure 9h may be dominated by magnetic aligning torque and contribute to the paleomagnetic record.

5.2. Detrital Hematite

Detrital hematite is a common magnetic mineral in sediments. Their very weak saturation magnetization and wide grain-size distribution make it difficult to quantify their concentration in sediments (Roberts et al., 2020). Thus,

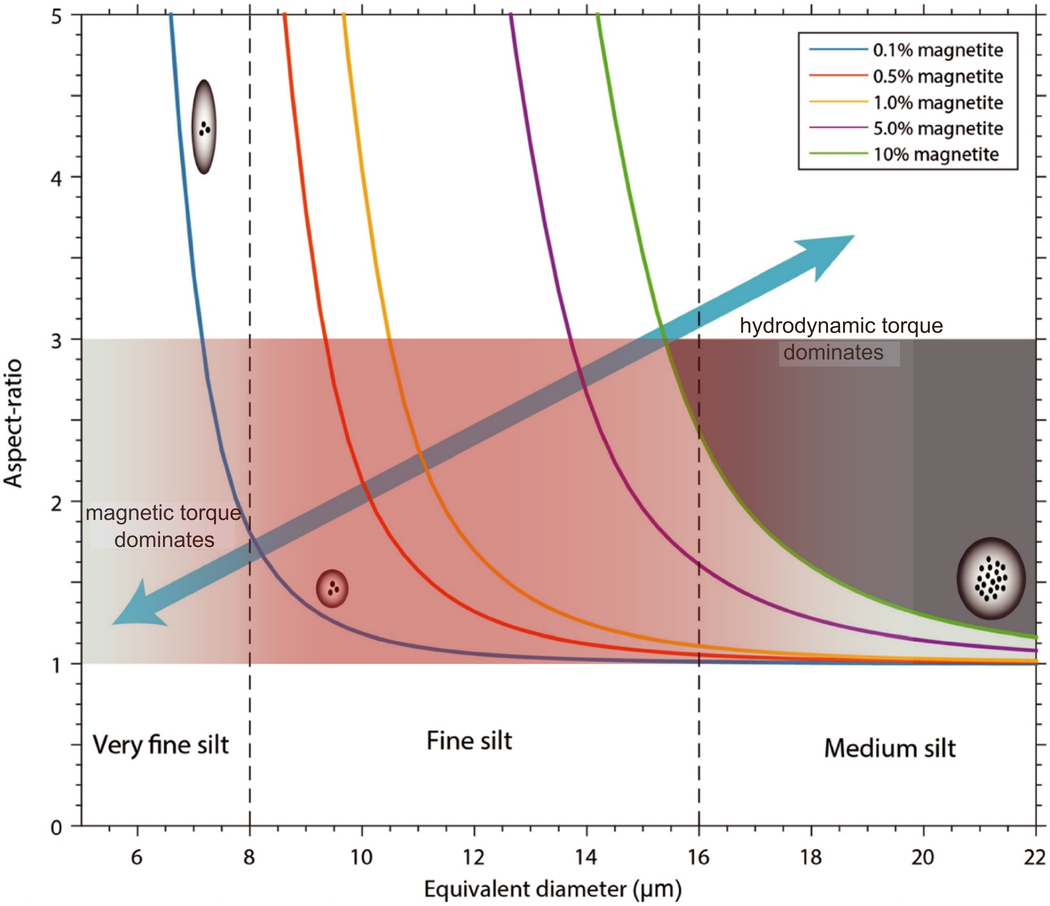

Figure 12. Model of depositional remanent magnetization (DRM) acquisition potential of silicate-hosted magnetic inclusions with various diameter and aspect-ratio of host silicates and magnetite concentration within silicates (modified from Chang, Roberts et al. (2016)). Aspect-ratio range of 1–3 is colored, in which most host silicate particles of the studied samples are expected to fall. Blue arrows indicate competing relationship between magnetic aligning torque and hydrodynamic torque. The area with a red hue indicates the approximate range of grain diameters and aspect ratios of host silicates in the studied sediments, which mainly occupies the region of hydrodynamic torque dominance in the right side of the magnetite concentration curve estimated for the studied samples (∼0.25%).

contributions of hematite to paleomagnetic records were often overlooked. Hematite was reported to be more resistive against reductive dissolution than magnetite based on distinct high-coercivity signals observed in reduced sediments (Abrajevitch et al., 2009; Abrajevitch & Kodama, 2011; Yamazaki et al., 2003). The higher stability of hematite to reductive dissolution suggests that relative concentration of hematite may become large for sediments in reduced environments. Furthermore, hematite exhibits a wide SD size range from about 30 nm to tens of μm (Banerjee, 1971; Jiang et al., 2022; Kletetschka & Wasilewski, 2002; Özdemir & Dunlop, 2014), which makes hematite in deep-sea sediments being mostly in the SD state. Thus, hematite is potentially important for paleomagnetic recording in reduced sediments.

The proportion of remanence carried by high-coercivity minerals is larger below the dissolution front of the studied sediments than above, as indicated by S-ratios (Figure 2b) and AF demagnetization behaviors of NRM and ARM (Figures S3a and S3b in Supporting Information S1). The SIRM fractions in Figure 8 show that the relative contribution of hematite to the SIRM is more than 30%. These results suggest that hematite may be a dominant carrier of NRM below the dissolution front. A decrease in the mean coercivity of hematite below the dissolution front indicated by the IRM component analysis (Figure 7) may be attributable to a decrease in the average grain size of hematite associated with diagenetic dissolution and/or cation substitutions. Hematite is known to have grain-size dependent coercivity (Jiang et al., 2022; Özdemir & Dunlop, 2014). Magnetic properties of hematite are also influenced by cation substitutions within the crystallographic structure, which can occur widely in natural hematite grains (Jiang et al., 2012, 2022).

Actual volumetric proportion of hematite to magnetite in the studied sediments is roughly estimated by dividing the ratio of their relative contributions to SIRM by the ratio of their stoichiometric volume-normalized saturation magnetizations; hematite is about 8 times more abundant in volume than magnetite even above the dissolution front. However, the sediments either above or below the dissolution front did not show rock-magnetic signals indicative of hematite, such as the Morin transition (Morin, 1950) in low-temperature magnetic measurements or the mixed kidney-shaped and ridge-type distributions in FORC diagrams (Roberts et al., 2021). The absence of such signals may be due to overwhelmingly stronger magnetization of coexisting magnetite in the relict magnetic mineral assemblages (Roberts et al., 2020, 2021). Alternatively, as Morin transition temperature of hematite is grain-size dependent (Jiang et al., 2022; Özdemir & Dunlop, 2014; Özdemir et al., 2008), Morrin transition signals are suppressed if the hematite grains have wide grain-size distribution as suggested by the large DP in the IRM decomposition. In addition, various degrees of cation substitution can also result in the suppression of the hematite signals (Jiang et al., 2022).

5.3. Contributions of Silicate-Hosted Magnetic Inclusions and Hematite to Paleomagnetic Records

Below the dissolution front, RPI was calculated from NRM normalized by ARM in a higher-coercivity (25–50 mT) window, where the remanence is estimated to be carried by silicate-hosted magnetic inclusions and part of hematite with lower coercivities. NRM/ARM_25–50 mT is comparable to NRM/ARM_10–25 mT above the dissolution front, which is carried mainly by detrital magnetite (Figure 10b).

Silicate-hosted magnetic inclusions possess a finer grain-size distribution and weaker magnetostatic interactions than unprotected detrital magnetite, as indicated by the FORC diagrams (Figure 6). These characteristics may lead higher ARM acquisition efficiency for magnetic inclusions compared to unprotected detrital magnetite. Considering that DRM acquisition efficiency of the silicate-hosted magnetic inclusions in the studied sediments is estimated to be relatively low as discussed in Section 5.1, NRM/ARM_25–50 mT below the dissolution front should be significantly lower than NRM/ARM_10–25 mT above the dissolution front. However, this is not supported by the observation. One possible interpretation is that the actual contribution of the magnetic inclusions to NRM is small and the NRM in the higher-coercivity (25–50 mT) window below the dissolution front is significantly carried by hematite of the lower coercivity tail.

Although the paleomagnetic direction and RPI were recovered from the remanence carried by magnetic components with coercivities lower than 80 mT, which is the highest AF demagnetization field applied in this study, potential contribution of hematite with the mean coercivity of ~175 mT to the paleomagnetic records should not be overlooked in the reduced sediments. Considering that the mean coercivity of silicate-hosted magnetic inclusions, ~62 mT from the IRM component analysis, is relatively close to that of magnetofossil, ~51 mT, NRM coercivity spectra should not exhibit a pronounced difference across the dissolution front if the magnetization below the dissolution front is mainly carried by the silicate-hosted magnetic inclusions. Conversely, the harder NRM coercivity (Figure S3a in Supporting Information S1) suggests the predominant contribution of hematite.

5.4. Oceanographic Implications

The depth of the dissolution front in core MR1402-PC3, 5.7 m, is shallower than that of core MR1402-PC4 taken ~250 km north of PC3, ~11.1 m (Li Jiaxi et al., 2022). This might be caused by higher organic matter input due to higher productivity associated with the site location of core MR1402-PC3 nearer to the equator. However, almost the same average sedimentation rates of the two cores, ~1.4 cm/kyr, do not support such interpretation. Dissolved oxygen concentration increases with depth in a water column below the oxygen minimum zone at ~1000 m in depth (Levin, 2003; Paulmier & Ruiz-Pino, 2009). The shallower water depth of core MR1402-PC3 places it in a less oxic environment, which may lead the progress of reductive diagenesis in shallower depths below the seafloor. A linear relationship between the depth of the dissolution front and the water depth of the coring sites was reported for sediments of the OJP by Tauxe and Shackleton (1994), and cores MR1402-PC3 and PC4 also follow this trend. The difference in bottom-water oxygen concentration may be a controlling factor of the depth of the dissolution front in sedimentary columns of the OJP sediments.

6. Conclusions

Our paleo- and rock magnetic study of sediment core MR1402-PC3 taken from the OJP has led the following conclusions.

1. The studied sediment core suffered reductive diagenesis, and the magnetite dissolution front occurs at 5.7 m in depth. Above the dissolution front, magnetofossil and detrital magnetite are the major remanence carriers contributing to the paleomagnetic records.
2. Below the dissolution front, magnetofossil and unprotected detrital magnetite were dissolved, while silicate-hosted magnetic inclusions and detrital hematite survived dissolution and carry 46%–63% and 21%–34% of SIRM, respectively. The contribution of silicate-hosted magnetic inclusions to NRM is estimated to be limited from the grain sizes of host silicates and the concentration of magnetic inclusions. Detrital hematite may be an important carrier of NRM below the dissolution front.
3. Magnetostratigraphy and RPI correlative to the global paleointensity stacks could be recovered even below the dissolution front. There is no significant gap between ARM-normalized RPIs calculated from a coercivity window from 10 to 25 mT above the dissolution front and those of a 25–50 mT window below. The former is considered to be carried mainly by unprotected detrital magnetite, whereas the latter could be largely carried by relict hematite.
4. Bottom water oxygen concentration may be a controlling factor of the depth of the dissolution front in sedimentary columns of the OJP sediment cores.

Our study implies that large numbers of legacy sediment cores that were excluded from paleomagnetic studies by reason of reduction diagenesis may be useful for future research.

Conflict of Interest

The authors declare no conflicts of interest relevant to this study.

Data Availability Statement

Paleo- and rock magnetic data of this study are available in Zenodo repository at https://doi.org/10.5281/zenodo.15770548 and https://doi.org/10.5281/zenodo.15770610 (Li Jiaxi et al., 2025a, 2025b).

Acknowledgments
We thank all onboard scientists, officers, and crew of R/V Mirai MR14-02 cruise and onshore personnel related to the cruise for cooperation in obtaining the sediment core, and Toshihiro Yoshimura and Haruka Takagi for help with onboard sampling. We also thank Yuhji Yamamoto for support of the paleo- and rock-magnetic measurements and data processing and for discussion, Yoichi Usui and Yosuke Miyairi for instructing the geochemical experimental procedures to extract silicate-hosted magnetic inclusions, Toshihiko Sugai and Ryuhei Sanjo for support of the grain size analysis, Chisato Anai for advice on the acetic acid treatment, Nobuhiro Ogawa for technical assistance of the TEM observations, and Juichiro Ashi for discussion. The manuscript was improved by the comments of two anonymous reviewers. This study was partly conducted under the cooperative research program of the Marine Core Research Institute, Kochi University (19A024, 19B022, 21A006, 21B006, 22A006, and 22B005), and supported by a Grant-in-Aid for Scientific Research (KAKENHI) of the Japan Society for the Promotion of Science (19H01997 and 23K03542) and the China Scholarship Council (202108050144).

References

Abrajevitch, A., & Kodama, K. (2011). Diagenetic sensitivity of paleoenvironmental proxies: A rock magnetic study of Australian continental margin sediments. *Geochemistry, Geophysics, Geosystems*, *12*(5). https://doi.org/10.1029/2010GC003481

Abrajevitch, A., van der Voo, R., & Rea, D. K. (2009). Variations in relative abundances of goethite and hematite in Bengal Fan sediments: Climatic vs. diagenetic signals. *Marine Geology*, *267*(3), 191–206. https://doi.org/10.1016/j.margeo.2009.10.010

Akai, J., Sato, T., & Okusa, S. (1991). TEM study on biogenic magnetite in deep-sea sediments from the Japan Sea and the Western Pacific Ocean. *Journal of Electron Microscopy*, *40*, 110–117.

Banerjee, S. K. (1971). New grain size limits for palaeomagnetic stability in haematite. *Nature; Physical Science*, *232*(27), 15–16. https://doi.org/10.1038/physci232015a0

Bazylinski, D. A., Garratt-Reed, A. J., & Frankel, R. B. (1994). Electron microscopic studies of magnetosomes in magnetotactic bacteria. *Microscopy Research and Technique*, *27*(5), 389–401. https://doi.org/10.1002/jemt.1070270505

Berner, R. A. (1980). *Early diagenesis: A theoretical approach*. Princeton University Press. Retrieved from http://www.jstor.org/stable/j.ctvx8b6p2

Berner, R. A. (1981). A new geochemical classification of sedimentary environments. *Journal of Sedimentary Research*, *51*(2), 359–365. https://doi.org/10.1306/212F7C7F-2B24-11D7-8648000102C1865D

Berner, R. A. (1984). Sedimentary pyrite formation: An update. *Geochimica et Cosmochimica Acta*, *48*(4), 605–615. https://doi.org/10.1016/0016-7037(84)90089-9

Blatt, H., Jones, R. L., & Charles, R. G. (1982). Separation of quartz and feldspars from mudrocks. *Journal of Sedimentary Research*, *52*(2), 660–661. https://doi.org/10.2110/jsr.52.660

Bloemendal, J., King, J. W., Hall, F. R., & Doh, S.-J. (1992). Rock magnetism of late Neogene and Pleistocene deep-sea sediments: Relationship to sediment source, diagenetic processes, and sediment lithology. *Journal of Geophysical Research: Solid Earth*, *97*(B4), 4361–4375. https://doi.org/10.1029/91jb03068

Bloemendal, J., King, J. W., Hunt, A., Demenocal, P. B., & Hayashida, A. (1993). Origin of the sedimentary magnetic record at Ocean Drilling Program Sites on the Owen Ridge, western Arabian Sea. *Journal of Geophysical Research: Solid Earth*, *98*(B3), 4199–4219. https://doi.org/10.1029/92JB02914

Bouilloux, A., Valet, J.-P., Bassinot, F., Joron, J.-L., Blanc-Valleron, M.-M., Moreno, E., et al. (2013). Diagenetic modulation of the magnetic properties in sediments from the Northern Indian Ocean. *Geochemistry, Geophysics, Geosystems*, *14*(9), 3779–3800. https://doi.org/10.1002/ggge.20234

Canfield, D. E., & Berner, R. A. (1987). Dissolution and pyritization of magnetite in anoxie marine sediments. *Geochimica et Cosmochimica Acta*, *51*(3), 645–659. https://doi.org/10.1016/0016-7037(87)90076-7

Chang, L., Bolton, C. T., Dekkers, M. J., Hayashida, A., Heslop, D., Krijgsman, W., et al. (2016). Asian monsoon modulation of nonsteady state diagenesis in hemipelagic marine sediments offshore of Japan. *Geochemistry, Geophysics, Geosystems*, *17*(11), 4383–4398. https://doi.org/10.1002/2016GC006344

Chang, L., Heslop, D., Roberts, A. P., Rey, D., & Mohamed, K. J. (2016). Discrimination of biogenic and detrital magnetite through a double Verwey transition temperature. *Journal of Geophysical Research: Solid Earth*, *121*(1), 3–14. https://doi.org/10.1002/2015JB012485

Chang, L., Hong, H., Bai, F., Wang, S., Pei, Z., Paterson, G. A., et al. (2021). Detrital remanent magnetization of single-crystal silicates with magnetic inclusions: Constraints from deposition experiments. *Geophysical Journal International*, *224*(3), 2001–2015. https://doi.org/10.1093/gji/ggaa559

Chang, L., Roberts, A. P., Heslop, D., Hayashida, A., Li, J., Zhao, X., et al. (2016). Widespread occurrence of silicate-hosted magnetic mineral inclusions in marine sediments and their contribution to paleomagnetic recording. *Journal of Geophysical Research: Solid Earth*, *121*(12), 8415–8431. https://doi.org/10.1002/2016JB013109

Chang, L., Roberts, A. P., Winklhofer, M., Heslop, D., Dekkers, M. J., Krijgsman, W., et al. (2014). Magnetic detection and characterization of biogenic magnetic minerals: A comparison of ferromagnetic resonance and first-order reversal curve diagrams. *Journal of Geophysical Research: Solid Earth*, *119*(8), 6136–6158. https://doi.org/10.1002/2014JB011213

Channell, J. E. T., Singer, B. S., & Jicha, B. R. (2020). Timing of Quaternary geomagnetic reversals and excursions in volcanic and sedimentary archives. *Quaternary Science Reviews*, *228*, 106114. https://doi.org/10.1016/J.QUASCIREV.2019.106114

Channell, J. E. T., Xuan, C., & Hodell, D. A. (2009). Stacking paleointensity and oxygen isotope data for the last 1.5 Myr (PISO-1500). *Earth and Planetary Science Letters*, *283*(1–4), 14–23. https://doi.org/10.1016/J.EPSL.2009.03.012

Chen, L., Heslop, D., Roberts, A. P., Chang, L., Zhao, X., McGregor, H. V., et al. (2017). Remanence acquisition efficiency in biogenic and detrital magnetite and recording of geomagnetic paleointensity. *Geochemistry, Geophysics, Geosystems*, *18*(4), 1435–1450. https://doi.org/10.1002/2016GC006753

Clayton, R. N., Rex, R. W., Syers, J. K., & Jackson, M. L. (1972). Oxygen isotope abundance in quartz from Pacific pelagic sediments. *Journal of Geophysical Research*, *77*(21), 3907–3915. https://doi.org/10.1029/JC077i021p03907

Dang, H., Wu, J., Xiong, Z., Qiao, P., Li, T., & Jian, Z. (2020). Orbital and sea-level changes regulate the iron-associated sediment supplies from Papua New Guinea to the equatorial Pacific. *Quaternary Science Reviews*, *239*, 106361. https://doi.org/10.1016/j.quascirev.2020.106361

Egli, R. (2004). Characterization of individual rock magnetic components by analysis of remanence curves. 2. Fundamental properties of coercivity distributions. *Physics and Chemistry of the Earth*, *29*(13–14), 851–867. https://doi.org/10.1016/j.pce.2004.04.001

Egli, R. (2006). Theoretical aspects of dipolar interactions and their appearance in first-order reversal curves of thermally activated single-domain particles. *Journal of Geophysical Research: Solid Earth*, *111*(B12). https://doi.org/10.1029/2006JB004567

Froelich, P. N., Klinkhammer, G. P., Bender, M. L., Luedtke, N. A., Heath, G. R., Cullen, D., et al. (1979). Early oxidation of organic matter in pelagic sediments of the eastern equatorial Atlantic: Suboxic diagenesis. *Geochimica et cosmochimica acta*, *43*(7), 1075–1090. https://doi.org/10.1016/0016-7037(79)90095-4

Heslop, D. (2015). Numerical strategies for magnetic mineral unmixing. *Earth-Science Reviews*, *150*, 256–284. https://doi.org/10.1016/j.earscirev.2015.07.007

Hong, H., Chang, L., Hayashida, A., Roberts, A. P., Heslop, D., Paterson, G. A., et al. (2019). Paleomagnetic recording efficiency of sedimentary magnetic mineral inclusions: Implications for relative paleointensity determinations. *Journal of Geophysical Research: Solid Earth*, *124*(7), 6267–6279. https://doi.org/10.1029/2018JB016859

Hounslow, M. W., & Maher, B. A. (1996). Quantitative extraction and analysis of carriers of magnetization in sediments. *Geophysical Journal International*, *124*(1), 57–74. https://doi.org/10.1111/j.1365-246X.1996.tb06352.x

Inoue, K., Yamazaki, T., & Usui, Y. (2021). Influence of magnetofossils on paleointensity estimations inferred from principal component analyses of first-order reversal curve diagrams for sediments from the western equatorial Pacific. *Geochemistry, Geophysics, Geosystems*, *22*(10), e2021GC010081. https://doi.org/10.1029/2021GC010081

Jiang, Z., Liu, Q., Barrón, V., Torrent, J., & Yu, Y. (2012). Magnetic discrimination between Al-substituted hematites synthesized by hydrothermal and thermal dehydration methods and its geological significance. *Journal of Geophysical Research: Solid Earth*, *117*(B2). https://doi.org/10.1029/2011JB008605

Jiang, Z., Liu, Q., Roberts, A. P., Dekkers, M. J., Barrón, V., Torrent, J., & Li, S. (2022). The magnetic and color reflectance properties of hematite: From Earth to Mars. *Reviews of Geophysics*, *60*(1), e2020RG000698. https://doi.org/10.1029/2020RG000698

Karlin, R., & Levi, S. (1983). Diagenesis of magnetic minerals in recent haemipelagic sediments. *Nature*, *303*(5915), 327–330. https://doi.org/10.1038/303327a0

King, J. W., Banerjee, S. K., & Marvin, J. (1983). A new rock-magnetic approach to selecting sediments for geomagnetic paleointensity studies: Application to paleointensity for the last 4000 years. *Journal of Geophysical Research*, *88*(B7), 5911–5921. https://doi.org/10.1029/JB088iB07p05911

Kirschvink, J. L. (1980). The least-squares line and plane and the analysis of palaeomagnetic data. *Geophysical Journal International*, *62*(3), 699–718. https://doi.org/10.1111/j.1365-246X.1980.tb02601.x

Kirschvink, J. L., Kobayashi-Kirschvink, A., & Woodford, B. J. (1992). Magnetite biomineralization in the human brain. *Proceedings of the National Academy of Sciences*, *89*(16), 7683–7687. https://doi.org/10.1073/pnas.89.16.7683

Kletetschka, G., & Wasilewski, P. J. (2002). Grain size limit for SD hematite. *Physics of the Earth and Planetary Interiors*, *129*(1–2), 173–179. https://doi.org/10.1016/S0031-9201(01)00271-0

Kok, Y. S., & Tauxe, L. (1999). A relative geomagnetic paleointensity stack from Ontong-Java Plateau sediments for the Matuyama. *Journal of Geophysical Research: Solid Earth*, *104*(B11), 25401–25413. https://doi.org/10.1029/1999JB900186

Larrasoaña, J. C., Roberts, A. P., Hayes, A., Wehausen, R., & Rohling, E. J. (2006). Detecting missing beats in the Mediterranean climate rhythm from magnetic identification of oxidized sapropels (Ocean Drilling Program Leg 160). *Physics of the Earth and Planetary Interiors*, *156*(3), 283–293. https://doi.org/10.1016/j.pepi.2005.04.017

Levin, L. A. (2003). Oxygen minimum zone benthos: Adaptation and community response to hypoxia. In R. N. Gibson & R. J. Atkinson (Eds.), *Oceanography and marine biology* (pp. 1–45). CRC Press.

Li, J., Menguy, N., Roberts, A. P., Gu, L., Leroy, E., Bourgon, J., et al. (2020). Bullet-shaped magnetite biomineralization within a magnetotactic deltaproteobacterium: Implications for magnetofossil identification. *Journal of Geophysical Research: Biogeosciences*, *125*(7), e2020JG005680. https://doi.org/10.1029/2020JG005680

Li, J., Pan, Y., Chen, G., Liu, Q., Tian, L., & Lin, W. (2009). Magnetite magnetosome and fragmental chain formation of Magnetospirillum magneticum AMB-1: Transmission electron microscopy and magnetic observations. *Geophysical Journal International*, *177*(1), 33–42. https://doi.org/10.1111/j.1365-246X.2009.04043.x

Li, J., Yamazaki, T., Sato, M., & Kuroda, J. (2025a). Rock- and paleomagnetic data of sediment core MR1402-PC3 taken from the Ontong Java Plateau [Dataset]. https://doi.org/10.5281/zenodo.15770548

Li, J., Yamazaki, T., Sato, M., & Kuroda, J. (2025b). Rock- and paleomagnetic data of sediment core MR1402-PC3 taken from the Ontong Java Plateau [Dataset]. https://doi.org/10.5281/zenodo.15770610

Li, J., Yamazaki, T., Usui, Y., Sagawa, T., Kubota, Y., & Kuroda, J. (2022). Understanding the role of biogenic magnetite in geomagnetic paleointensity recording: Insights from Ontong Java Plateau sediments. *Journal of Geophysical Research: Solid Earth*, *127*(6), e2022JB024387. https://doi.org/10.1029/2022JB024387

Lyle, M. (1983). The brown-green color transition in marine sediments: A marker of the Fe(III)-Fe(II) redox boundary1. *Limnology & Oceanography*, *28*(5), 1026–1033. https://doi.org/10.4319/lo.1983.28.5.1026

Morin, F. J. (1950). Magnetic susceptibility of αFe_2O_3 and αFe_2O_3 with added Titanium. *Physical Review*, *78*(6), 819–820. https://doi.org/10.1103/PhysRev.78.819.2

O'Reilly, W. (1984). *Rock and mineral magnetism*. Blackie. Retrieved from http://lib.ugent.be/catalog/rug

Ouyang, T., Heslop, D., Roberts, A. P., Tian, C., Zhu, Z., Qiu, Y., & Peng, X. (2014). Variable remanence acquisition efficiency in sediments containing biogenic and detrital magnetites: Implications for relative paleointensity signal recording. *Geochemistry, Geophysics, Geosystems*, *15*(7), 2780–2796. https://doi.org/10.1002/2014GC005301

Özdemir, Ö., & Dunlop, D. J. (2014). Hysteresis and coercivity of hematite. *Journal of Geophysical Research: Solid Earth*, *119*(4), 2582–2594. https://doi.org/10.1002/2013JB010739

Özdemir, Ö., Dunlop, D. J., & Berquó, T. S. (2008). Morin transition in hematite: Size dependence and thermal hysteresis. *Geochemistry, Geophysics, Geosystems*, *9*(10). https://doi.org/10.1029/2008GC002110

Pan, Y., Petersen, N., Winklhofer, M., Davila, A. F., Liu, Q., Frederichs, T., et al. (2005). Rock magnetic properties of uncultured magnetotactic bacteria. *Earth and Planetary Science Letters*, *237*(3–4), 311–325. https://doi.org/10.1016/j.epsl.2005.06.029

Paulmier, A., & Ruiz-Pino, D. (2009). Oxygen minimum zones (OMZs) in the modern ocean. *Progress in Oceanography*, *80*(3), 113–128. https://doi.org/10.1016/j.pocean.2008.08.001

Poulton, S. W., Krom, M. D., & Raiswell, R. (2004). A revised scheme for the reactivity of iron (oxyhydr)oxide minerals towards dissolved sulfide. *Geochimica et Cosmochimica Acta*, *68*(18), 3703–3715. https://doi.org/10.1016/J.GCA.2004.03.012

Roberts, A. P. (2015). Magnetic mineral diagenesis. *Earth-Science Reviews*, *151*, 1–47. https://doi.org/10.1016/j.earscirev.2015.09.010

Roberts, A. P., Chang, L., Heslop, D., Florindo, F., & Larrasoaa, J. C. (2012). Searching for single domain magnetite in the "pseudo-single-domain" sedimentary haystack: Implications of biogenic magnetite preservation for sediment magnetism and relative paleointensity determinations. *Journal of Geophysical Research: Solid Earth*, *117*(8). https://doi.org/10.1029/2012JB009412

Roberts, A. P., Florindo, F., Chang, L., Heslop, D., Jovane, L., & Larrasoaña, J. C. (2013). Magnetic properties of pelagic marine carbonates. *Earth-Science Reviews*, *127*, 111–139. https://doi.org/10.1016/j.earscirev.2013.09.009

Roberts, A. P., Florindo, F., Villa, G., Chang, L., Jovane, L., Bohaty, S. M., et al. (2011). Magnetotactic bacterial abundance in pelagic marine environments is limited by organic carbon flux and availability of dissolved iron. *Earth and Planetary Science Letters*, *310*(3), 441–452. https://doi.org/10.1016/j.epsl.2011.08.011

Roberts, A. P., Heslop, D., Zhao, X., & Pike, C. R. (2014). Understanding fine magnetic particle systems through use of first-order reversal curve diagrams. *Reviews of Geophysics*, *52*(4), 557–602. https://doi.org/10.1002/2014RG000462

Roberts, A. P., Zhao, X., Harrison, R. J., Heslop, D., Muxworthy, A. R., Rowan, C. J., et al. (2018). Signatures of reductive magnetic mineral diagenesis from unmixing of first-order reversal curves. *Journal of Geophysical Research: Solid Earth*, *123*(6), 4500–4522. https://doi.org/10.1029/2018JB015706

Roberts, A. P., Zhao, X., Heslop, D., Abrajevitch, A., Chen, Y.-H., Hu, P., et al. (2020). Hematite (α-Fe_2O_3) quantification in sedimentary magnetism: Limitations of existing proxies and ways forward. *Geoscience Letters*, *7*(1), 8. https://doi.org/10.1186/s40562-020-00157-5

Roberts, A. P., Zhao, X., Hu, P., Abrajevitch, A., Chen, Y.-H., Harrison, R. J., et al. (2021). Magnetic domain state and anisotropy in hematite (α-Fe_2O_3) from first-order reversal curve diagrams. *Journal of Geophysical Research: Solid Earth*, *126*(12), e2021JB023027. https://doi.org/10.1029/2021JB023027

Rowan, C. J., Roberts, A. P., & Broadbent, T. (2009). Reductive diagenesis, magnetite dissolution, greigite growth and paleomagnetic smoothing in marine sediments: A new view. *Earth and Planetary Science Letters*, *277*(1), 223–235. https://doi.org/10.1016/j.epsl.2008.10.016

Singer, B. S. (2014). A Quaternary geomagnetic instability time scale. *Quaternary Geochronology*, *21*(1), 29–52. https://doi.org/10.1016/J.QUAGEO.2013.10.003

Stevens, R. L. (1991). Grain-size distribution of quartz and feldspar extracts and implications for flocculation processes. *Geo-Marine Letters*, *11*(3), 162–165. https://doi.org/10.1007/BF02431004

Suganuma, Y., Okada, M., Horie, K., Kaiden, H., Takehara, M., Senda, R., et al. (2015). Age of Matuyama-Brunhes boundary constrained by U-Rb zircon dating of a widespread tephra. *Geology*, *43*(6), 491–494. https://doi.org/10.1130/G36625.1

Syers, J. K., Chapman, S. L., Jackson, M. L., Rex, R. W., & Clayton, R. N. (1968). Quartz isolation from rocks, sediments and soils for determination of oxygen isotopes composition. *Geochimica et Cosmochimica Acta*, *32*(9), 1022–1025. https://doi.org/10.1016/0016-7037(68)90067-7

Tarduno, J. A., Tian, W., & Wilkison, S. (1998). Biogeochemical remanent magnetization in pelagic sediments of the western equatorial Pacific Ocean. *Geophysical Research Letters*, *25*(21), 3987–3990. https://doi.org/10.1029/1998GL900079

Tarduno, J. A., & Wilkison, S. L. (1996). Non-steady state magnetic mineral reduction, chemical lock-in, and delayed remanence acquisition in pelagic sediments. *Earth and Planetary Science Letters*, *144*(3), 315–326. https://doi.org/10.1016/S0012-821X(96)00174-4

Tauxe, L. (1993). Sedimentary records of relative paleointensity of the geomagnetic field: Theory and practice. *Reviews of Geophysics*, *31*(3), 319–354. https://doi.org/10.1029/93RG01771

Tauxe, L., Pick, T., & Kok, Y. S. (1995). Relative paleointensity in sediments: A Pseudo-Thellier approach. *Geophysical Research Letters*, *22*(21), 2885–2888. https://doi.org/10.1029/95GL03166

Tauxe, L., & Shackleton, N. J. (1994). Relative palaeointensity records from the Ontong-Java Plateau. *Geophysical Journal International*, *117*(3), 769–782. https://doi.org/10.1111/j.1365-246X.1994.tb02469.x

Thomas-Keprta, K. L., Bazylinski, D. A., Kirschvink, J. L., Clemett, S. J., McKay, D. S., Wentworth, S. J., et al. (2000). Elongated prismatic magnetite crystals in ALH84001 carbonate globules: Potential Martian magnetofossils. *Geochimica et Cosmochimica Acta*, *64*(23), 4049–4081. https://doi.org/10.1016/S0016-7037(00)00481-6

Thomson, J., Wilson, T. R. S., Culkin, F., & Hydes, D. J. (1984). Non-steady state diagenetic record in eastern equatorial Atlantic sediments. *Earth and Planetary Science Letters*, *71*(1), 23–30. https://doi.org/10.1016/0012-821X(84)90049-9

Usui, Y., Shimono, T., & Yamazaki, T. (2018). Rock magnetism of quartz and feldspars chemically separated from pelagic red clay: A new approach to provenance study. *Earth Planets and Space*, *70*(1), 153. https://doi.org/10.1186/s40623-018-0918-1

Usui, Y., & Yamazaki, T. (2021). Non-chained, non-interacting, stable single-domain magnetite octahedra in deep-sea red clay: A new type of magnetofossil? *Geochemistry, Geophysics, Geosystems*, *22*(7), e2021GC009770. https://doi.org/10.1029/2021GC009770

Valencia, M. J. (1973). Calcium carbonate and gross-size analysis of surface sediments, western equatorial Pacific. *Pacific Science*, *27*, 290–303.

Verwey, E. J. W. (1939). Electronic conduction of magnetite (Fe_3O_4) and its transition point at low temperatures. *Nature*, *144*(3642), 327–328. https://doi.org/10.1038/144327b0

Wessel, P., Luis, J. F., Uieda, L., Scharroo, R., Wobbe, F., Smith, W. H. F., & Tian, D. (2019). The generic mapping tools version 6. *Geochemistry, Geophysics, Geosystems*, *20*(11), 5556–5564. https://doi.org/10.1029/2019GC008515

Yamamoto, Y., Yamazaki, T., Kanamatsu, T., Ioka, N., & Mishima, T. (2007). Relative paleointensity stack during the last 250 kyr in the northwest Pacific. *Journal of Geophysical Research: Solid Earth*, *112*(B1). https://doi.org/10.1029/2006JB004477

Yamazaki, T. (2008). Magnetostatic interactions in deep-sea sediments inferred from first-order reversal curve diagrams: Implications for relative paleointensity normalization. *Geochemistry, Geophysics, Geosystems*, *9*(2). https://doi.org/10.1029/2007GC001797

Yamazaki, T. (2009). Environmental magnetism of Pleistocene sediments in the North Pacific and Ontong-Java Plateau: Temporal variations of detrital and biogenic components. *Geochemistry, Geophysics, Geosystems*, *10*(7). https://doi.org/10.1029/2009GC002413

Yamazaki, T. (2020). Reductive dissolution of biogenic magnetite. *Earth Planets and Space*, *72*(1), 150. https://doi.org/10.1186/s40623-020-01290-3

Yamazaki, T., Abdeldayem, A. L., & Ikehara, K. (2003). Rock-magnetic changes with reduction diagenesis in Japan Sea sediments and preservation of geomagnetic secular variation in inclination during the last 30,000 years. *Earth Planets and Space*, *55*(6), 327–340. https://doi.org/10.1186/BF03351766

Yamazaki, T., Fu, W., Shimono, T., & Usui, Y. (2020). Unmixing biogenic and terrigenous magnetic mineral components in red clay of the Pacific Ocean using principal component analyses of first-order reversal curve diagrams and paleoenvironmental implications. *Earth Planets and Space*, *72*(1), 120. https://doi.org/10.1186/s40623-020-01248-5

Yamazaki, T., & Ikehara, M. (2012). Origin of magnetic mineral concentration variation in the Southern Ocean. *Paleoceanography*, *27*(2). https://doi.org/10.1029/2011PA002271

Yamazaki, T., Li, J., Shimono, T., & Kanamatsu, T. (2023). Difference in relative paleointensity recording efficiency of magnetic mineral constituents in a sediment core off Chile. *Journal of Geophysical Research: Solid Earth*, *128*(8), e2023JB026816. https://doi.org/10.1029/2023JB026816

Yamazaki, T., & Shimono, T. (2013). Abundant bacterial magnetite occurrence in oxic red clay. *Geology*, *41*(11), 1191–1194. https://doi.org/10.1130/G34782.1

Yamazaki, T., & Solheid, P. (2011). Maghemite-to-magnetite reduction across the Fe-redox boundary in a sediment core from the Ontong-Java Plateau: Influence on relative palaeointensity estimation and environmental magnetic application. *Geophysical Journal International*, *185*(3), 1243–1254. https://doi.org/10.1111/j.1365-246X.2011.05021.x

Yamazaki, T., Suzuki, Y., Kouduka, M., & Kawamura, N. (2019). Dependence of bacterial magnetosome morphology on chemical conditions in deep-sea sediments. *Earth and Planetary Science Letters*, *513*, 135–143. https://doi.org/10.1016/j.epsl.2019.02.015

Yamazaki, T., Yamamoto, Y., Acton, G., Guidry, E. P., & Richter, C. (2013). Rock-magnetic artifacts on long-term relative paleointensity variations in sediments. *Geochemistry, Geophysics, Geosystems*, *14*(1), 29–43. https://doi.org/10.1002/ggge.20064

Zhang, Q., Roberts, A. P., Ge, S., Liu, Y., Liu, J., Liu, S., et al. (2022). Interpretation of anhysteretic remanent magnetization carriers in magnetofossil-rich marine sediments. *Journal of Geophysical Research: Solid Earth*, *127*(11), e2022JB024432. https://doi.org/10.1029/2022JB024432

References From the Supporting Information

Egli, R. (2013). VARIFORC: An optimized protocol for calculating non-regular first-order reversal curve (FORC) diagrams. *Global and Planetary Change*, *110*, 302–320. https://doi.org/10.1016/j.gloplacha.2013.08.003

Gendler, T. S., Shcherbakov, V. P., Dekkers, M. J., Gapeev, A. K., Gribov, S. K., & McClelland, E. (2005). The lepidocrocite–maghemite–haematite reaction chain—I. Acquisition of chemical remanent magnetization by maghemite, its magnetic properties and thermal stability. *Geophysical Journal International*, *160*(3), 815–832. https://doi.org/10.1111/j.1365-246X.2005.02550.x

Harrison, R. J., & Feinberg, J. M. (2008). FORCinel: An improved algorithm for calculating first-order reversal curve distributions using locally weighted regression smoothing. *Geochemistry, Geophysics, Geosystems*, *9*(5). https://doi.org/10.1029/2008GC001987

Hanesch, M., Stanjek, H., & Petersen, N. (2006). Thermomagnetic measurements of soil iron minerals: The role of organic carbon. *Geophysical Journal International*, *165*(1), 53–61. https://doi.org/10.1111/j.1365-246X.2006.02933.x

Hirt, A. M., Banin, A., & Gehring, A. U. (1993). Thermal generation of ferromagnetic minerals from iron-enriched smectites. *Geophysical Journal International*, *115*(3), 1161–1168. https://doi.org/10.1111/j.1365-246X.1993.tb01518.x

Hu, G., Dam-Johansen, K., Wedel, S., & Hansen, J. P. (2006). Decomposition and oxidation of pyrite. *Progress in Energy and Combustion Science*, *32*(3), 295–314. https://doi.org/10.1016/j.pecs.2005.11.004

Lowrie, W. (1990). Identification of ferromagnetic minerals in a rock by coercivity and unblocking temperature properties. *Geophysical Research Letters*, *17*(2), 159–162. https://doi.org/10.1029/GL017i002p00159

Lowrie, W., & Heller, F. (1982). Magnetic properties of marine limestones. *Reviews of Geophysics*, *20*(2), 171–192. https://doi.org/10.1029/RG020i002p00171

Maxbauer, D. P., Feinberg, J. M., & Fox, D. L. (2016). MAX UnMix: A web application for unmixing magnetic coercivity distributions. *Computers & Geosciences*, *95*, 140–145. https://doi.org/10.1016/j.cageo.2016.07.009

Prasad, A., Singru, R. M., & Biswas, A. K. (1985). Study of the roasting of pyrite minerals by Mössbauer spectroscopy. *Physica Status Solidi A*, *87*(1), 267–271. https://doi.org/10.1002/pssa.2210870126

Robertson, D. J., & France, D. E. (1994). Discrimination of remanence-carrying minerals in mixtures, using isothermal remanent magnetisation acquisition curves. *Physics of the Earth and Planetary Interiors*, *82*(3), 223–234. https://doi.org/10.1016/0031-9201(94)90074-4

Yamamoto, Y., Fukami, H., & Lippert, P. C. (2022). Eocene relative paleointensity of the geomagnetic field from Integrated Ocean Drilling Program Site U1403 and U1408 sediments in the northwest Atlantic. *Earth and Planetary Science Letters*, *584*, 117518. https://doi.org/10.1016/j.epsl.2022.117518

Erratum

The originally published version of this article contained a typographical error. In the fifth sentence of the first paragraph of Section 4.4, “magnetic extracts between 8.6 and 13.32 m” has been corrected as follows: “magnetic extracts from 8.6 and 13.32 m.” This may be considered the authoritative version of record.